PAPER • OPEN ACCESS

Emergence of stationary many-body entanglement in driven-dissipative Rydberg lattice gases

To cite this article: Sun Kyung Lee *et al* 2015 *New J. Phys.* **17** 113053

New Journal of Physics
The open access journal at the forefront of physics

Deutsche Physikalische Gesellschaft DPG
IOP Institute of Physics

Published in partnership with: Deutsche Physikalische Gesellschaft and the Institute of Physics

OPEN ACCESS

RECEIVED
1 September 2015

REVISED
15 October 2015

ACCEPTED FOR PUBLICATION
28 October 2015

PUBLISHED
24 November 2015

PAPER

Emergence of stationary many-body entanglement in driven-dissipative Rydberg lattice gases

Sun Kyung Lee[1], **Jaeyoon Cho**[2] **and K S Choi**[3,4,5]

[1] Department of Physics & Astronomy and Center for Theoretical Physics, Seoul National University, Seoul 151-747, Korea
[2] School of Computational Science, Korea Institute for Advanced Study, Seoul 130-722, Korea
[3] Institute for Quantum Computing and Department of Physics & Astronomy, University of Waterloo, Waterloo, Ontario N2L 3G1, Canada
[4] Perimeter Institute for Theoretical Physics, Waterloo, Ontario N2L 2Y5, Canada
[5] Center for Quantum Information, Korea Institute of Science and Technology, Seoul 136-791, Korea

E-mail: kyung.choi@uwaterloo.ca

Keywords: quantum-reservoir engineering, quantum many-body physics, steady-state entanglement, non-equilibrium quantum dynamics, Rydberg atoms, quantum information science, quantum optics

Abstract

Non-equilibrium quantum dynamics represents an emerging paradigm for condensed matter physics, quantum information science, and statistical mechanics. Strongly interacting Rydberg atoms offer an attractive platform to examine driven-dissipative dynamics of quantum spin models with long-range order. Here, we explore the conditions under which stationary many-body entanglement persists with near-unit fidelity and high scalability. In our approach, coherent many-body dynamics is driven by Rydberg-mediated laser transitions, while atoms at the lattice boundary locally reduce the entropy of the many-body system. Surprisingly, the many-body entanglement is established by continuously evolving a locally dissipative Rydberg system towards the steady state, precisely as with optical pumping. We characterize the dynamics of multipartite entanglement in an one-dimensional lattice by way of quantum uncertainty relations, and demonstrate the long-range behavior of the stationary entanglement with finite-size scaling. Our work opens a route towards dissipative preparation of many-body entanglement with unprecedented scaling behavior.

1. Introduction

Quantum control of *open* many-body systems has become a major theme in the quest to explore new physics at the interface between condensed matter physics, quantum information science, and statistical mechanics [1–5]. The ability to control the many-body interactions and their dissipative processes has been identified as a powerful resource for the preparation of steady-state entanglement [6–14, 16–18] and the investigation of noise-driven quantum phase transitions [2, 19, 20]. Indeed, quantum-reservoir engineering provides the framework for dissipative quantum computation [3, 4] and communication [15] with built-in fault-tolerance. Furthermore, open system dynamics offers new prospectives to the relationship between entanglement and quantum thermodynamics [5].

Laser-driven Rydberg atoms offer unique possibilities for creating and manipulating open quantum systems $\hat{\rho}$ of dipolar interacting spin models [21–23]. By exciting N atoms to high-lying Rydberg states, strong and long-range interactions between the Rydberg atoms can be exploited to induce spin–spin interactions, whereas atoms comprising the many-body state can couple to their local radiative reservoirs by spontaneous emission [24]. The competition between the coherent and incoherent dynamics can drive the system to bipartite entangled states for two atoms [25, 26] and novel states of matter for a mesoscopic number of atoms, exhibiting topological order, glassiness, and crystallization dynamics [27–35]. Remarkably, the basic primitives behind such a principle have been demonstrated in the laboratory by several groups [36–41].

Despite the tantalizing prospects of quantum-reservoir engineering, the main obstacle has been that local decoherence (e.g., spontaneous emission) generally destroys the global entanglement of the system. Most

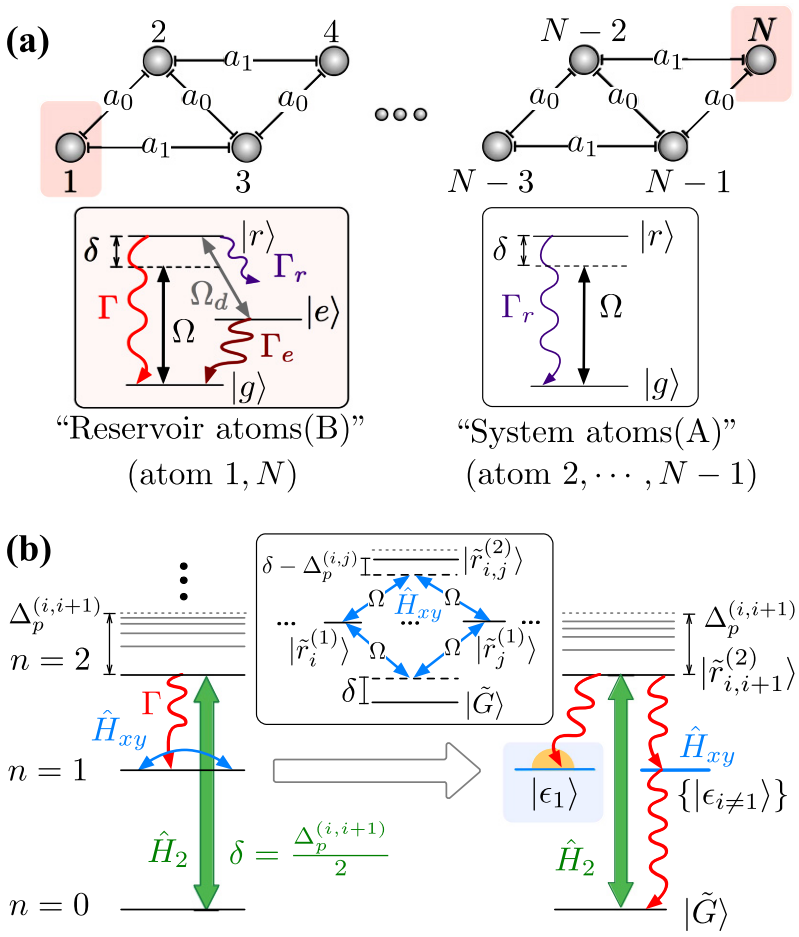

Figure 1. Production of stationary entanglement with Rydberg atoms in 1D lattice. (a) Schematic of optically driven, dissipative Rydberg atoms in a 1D staggered triangular lattice. Distances a_0 and a_1 are defined between spins in neighbor and next-neighbor configurations. Inset (i) the decay rates $\Gamma_{1,N} = \Gamma \gg \Gamma_r$ for the edge atoms are enhanced by mixing the Rydberg states $|r\rangle$ with short-lived $|e\rangle$ with local fields (Rabi frequency Ω_d) (appendix A). Inset (ii) atoms are pumped by a single, global driving field (Rabi frequency Ω) with detuning δ. (b) Rydberg blockaded atomic structure showing a rich family of anharmonic levels with level shifts $\Delta_{\rm p}^{(i,j)}$ for the Rydberg state $|\tilde{r}_{i,j}^{(2)}\rangle = |g\cdots r_i\cdots r_j\cdots g\rangle$, separated by subspace n. (Left) Two-photon process $\hat{H}_2$ optically pumps the population to the $n=1$ manifold. (Middle) XY Hamiltonian $\hat{H}_{xy}$ dictates the delocalization dynamics within the $n=1$ subspace. J_{ij} is driven by Raman transitions $|\tilde{r}_i^{(1)}\rangle \leftrightarrow |\tilde{r}_j^{(1)}\rangle$ with detuning δ ($\delta - \Delta_{\rm p}^{(i,j)}$) through intermediate state $|\tilde{G}\rangle$ ($|\tilde{r}_{i,j}^{(2)}\rangle$), while $\tilde{\Delta}_{\rm ls}^{(i)}$ is induced by light shifts. (Right) For $\delta = \Delta_{\rm p}^{(i,i+1)}/2$, atoms are dissipatively driven to the target eigenstate $|\epsilon_1\rangle = \sum_{i\in A}|\tilde{r}_i^{(1)}\rangle_A \otimes |g\cdots g\rangle_B$ with locally enhanced decoherence for atoms B.

proposals reported to date thereby achieve the required 'non-local' jump operator by way of collective system-bath coupling in order to suppress the information loss by local dissipation [6–14, 16–18]. In practice, such a coupling is achieved in the highly challenging, strong coupling regime for an array of qubits interacting with a common reservoir (e.g., cavity mode). Furthermore, for $N > 2$, the inherently local nature of the driving fields hardly allows only a single entangled state to be distinctively separated from the coupling to the reservoir, which enforces the introduction of auxiliary coherent manipulations and multiple time-steps of quantum gates and dissipations to single out a particular entangled state from a broader subspace [2, 11, 28], diluting the very nature of quantum-reservoir engineering. Such a challenge is further complicated by the characterization of entanglement for many-body states $\hat{\rho}(t)$ under evolution [1, 42–45].

Here, we explore such many-body entangled states persisting with high fidelity in the stationary limit for laser-driven Rydberg atoms in a lattice under *locally* engineered dissipation. As illustrated in figure 1, our protocol conceptually begins by globally pumping regularly arranged Rydberg atoms ($A \oplus B$) with a driving field Ω, where the lattice is separated into two partitions A, B. Rydberg excitation coherently delocalizes within the subspace defined by 'system' atoms A, while 'reservoir' atoms B at the lattice boundary serve as an entropy sink for A with local fields that enhance the spontaneous decay. By preparing a dark state in the Markovian dynamics, the atomic sample $\hat{\rho}(t)$ evolves towards the entangled steady state in the form of an eigenstate $|\epsilon_1\rangle = |W\rangle_A \otimes |g\cdots g\rangle_B$ of a lattice Hamiltonian $\hat{H}_{xy}$ in the single-excitation subspace, where $|W\rangle_A$ ($|g\cdots g\rangle_B$) is a

W-like entangled state (ground state) for A (B). The genuine multipartite entanglement for $\hat{\rho}(t)$ is unambiguously detected by the quantum uncertainty relations [46–48]. We find that steady-state W-state persists indefinitely with near-unit fidelity $F \geqslant 0.99$, and that entanglement depth k shows favorable scaling relative to its system size, reaching 'hectapartite'($k = 100$) entanglement for $N = 126$ atoms. Unlike all previous methods with auxiliary unitary and time-sequential dissipative manipulations [6–14, 16–18], the many-body entanglement in our protocol emerges purely out of the open system dynamics in a *time-independent*, *continuous* fashion with *local* decoherence, precisely as with optical pumping. Our method thereby allows the scalable production of stationary many-body entanglement with Rydberg atoms through locally engineered decoherence, where long-range entanglement extends well beyond the blockade radius.

2. Driven-dissipative preparation of many-body entangled states

2.1. Schematics

We consider many-body states of N atoms configured in a lattice (see figure 1(a)), irradiated by a uniform driving field Ω that couples the atomic ground state $|g\rangle$ to the highly excited Rydberg state $|r\rangle$ with detuning δ. A pair of atoms i, j in the Rydberg state at lattice sites $\vec{x}_i$, $\vec{x}_j$ couple each other via the potential $\Delta_{\rm p}^{(ij)} = C_{\rm p}\,|\vec{x}_i - \vec{x}_j|^{-p}$ with power-law scaling where $C_{\rm p}$ is the dipolar interaction coefficient, for which we take $p = 6$ for the van der Waals (vdW) regime of blockade shifts [24]. In a frame rotating with the laser frequency, the Hamiltonian is given by

$$\hat{H} = \sum_{i=1}^{N}\left(\delta\hat{\sigma}_{rr}^{(i)} + \Omega\hat{\sigma}_{x}^{(i)}\right) - \sum_{\langle i,j\rangle}^{N}\Delta_{\rm p}^{(ij)}\hat{\sigma}_{rr}^{(i)}\hat{\sigma}_{rr}^{(j)}, \tag{1}$$

where $\hat{\sigma}_{\mu\mu}^{(i)} = |\mu\rangle_i\langle\mu|$ is the projection operator for states $|\mu\rangle$ with $\mu \in \{g, r\}$, and $\hat{\sigma}_m^{(i)}$ are the canonical Pauli operators for atom i with $m \in \{x, y, z, \pm\}$.$\langle i, j\rangle$ denotes the sum over all $i \neq j$. In the following, we denote the ground state ($n = 0$) as $|\tilde{G}\rangle = |g\cdots g\rangle$, the singly excited ($n = 1$) states as $|\tilde{r}_i^{(1)}\rangle = |g_1\cdots r_i\cdots g_N\rangle$, and the doubly excited ($n = 2$) states as $|\tilde{r}_{ij}^{(2)}\rangle = |g_1\cdots r_i\cdots r_j\cdots g_N\rangle$ with the subspaces separated by the total number spin excitations $n = \sum_i\langle\hat{\sigma}_{rr}^{(i)}\rangle$.

The open many-body dynamics for the atomic state $\hat{\rho}$ is governed by a Markovian master equation $\dot{\hat{\rho}} = -\mathrm{i}[\hat{H}, \hat{\rho}] + \mathcal{L}\hat{\rho}$ with the Lindblad superoperators $\mathcal{L}\hat{\rho} = \sum_i \frac{\Gamma_i}{2}(2\hat{\sigma}_-^{(i)}\hat{\rho}\hat{\sigma}_+^{(i)} - \{\hat{\sigma}_+^{(i)}\hat{\sigma}_-^{(i)}, \hat{\rho}\})$ for the atomic coupling to their local radiative reservoirs. In order to allow the jump $n \to n - 1$, as employed for imaging ultracold Rydberg atoms [38] and derived in the appendix A, we can arbitrarily set the decay rate $\Gamma_i \simeq 4\,|\Omega_d|^2/\Gamma_e$ relative to its free-space rate Γ_r by coherently mixing the Rydberg level $|r\rangle$ and a rapidly decaying $|e\rangle$ with local field represented by its Rabi frequency Ω_d, where Γ_e is the decay rate of $|e\rangle$ (inset of figure 1). In practice, the short-lived state $|e\rangle$ can be a low-lying excited state (see appendix G).

2.2. Rydberg-mediated laser transitions and local decoherence

As shown by figure 1(b), our protocol starts by globally applying a single, global driving field of Rabi frequency Ω to all atoms $\{1\cdots N\}$ with detuning $\delta = \Delta_{\rm p}^{(i,i+1)}/2$. This field plays two roles. First, it drives the population in $|\tilde{G}\rangle$ to the $n = 2$ subspace via two-photon Raman resonance $\hat{H}_2$ (figures 1(b)). With the anharmonic Rydberg spectrum (see appendix B), higher-order transition $n \to n + 2$ for $n \geqslant 1$ is suppressed for moderate N, as the long-range nature of the van der Waals interaction $\Delta_{\rm p}^{(ij)}$ lifts all levels in $n \geqslant 3$ out of the two-photon resonance. This is enabled by having the blockade shifts much greater than power broadening of two-photon resonance ($\Delta_{\rm p}^{(ij)} > w_d^{(2)}$), where $w_d^{(2)}$ is the power-broadened linewidth for the two-photon transition as $w_d^{(2)} \simeq 2\sqrt{2}\,\Omega^2/\delta$. The net result along with the spontaneous decay is that the population is optically pumped into the single-excitation ($n = 1$) subspace (appendices B and C) for an atomic sample spread over a region L beyond the blockade distance $d_B = \sqrt[6]{C_{\rm p}/w_d}$, where $w_d \simeq \sqrt{2}\,\Omega$ is the power-broadened linewidth for the single-photon transition $n = 0 \leftrightarrow n = 1$.

The second role of Ω is to generate the necessary Raman couplings J_{ij} and light shifts $\bar{\Delta}_{\rm ls}^{(i)}$ within the $n = 1$ subspace (figure 1(b) inset) to physically realize the XY spin model H_{xy}. By adiabatically eliminating $|\tilde{G}\rangle$ and $|\tilde{r}_{ij}^{(2)}\rangle$ in the off-resonant limit $|\delta - \Delta_{\rm p}^{(ij)}| \gg w_d$, and obtain an effective Hamiltonian

$$\hat{H}_{xy} = \sum_{\langle i,j\rangle} J_{ij}\left(\hat{\sigma}_+^{(i)}\hat{\sigma}_-^{(j)} + \hat{\sigma}_-^{(i)}\hat{\sigma}_+^{(j)}\right) - \sum_{i=1}\bar{\Delta}_{\rm ls}^{(i)}\hat{\sigma}_{rr}^{(i)}, \tag{2}$$

in the single-excitation manifold. The nonlocal Raman transitions $J_{i,i+x}$ between $|\tilde{r}_i^{(1)}\rangle \leftrightarrow |\tilde{r}_{i+x}^{(1)}\rangle$ occur off-resonantly via virtual levels near $|\tilde{r}_{i,i+x}^{(2)}\rangle$ and $|\tilde{G}\rangle$, thereby providing the 'hopping' terms J_{ij} between sites i, $i + x$, while the light shift terms $\bar{\Delta}_{\rm ls}^{(i)}$ play the role of local 'magnetic' field of the XY Hamiltonian. After adiabatic

eliminations of $|\tilde{r}^{(2)}_{i,i+x}\rangle$ and $|\tilde{G}\rangle$, we obtain $J_{ij} = \frac{\Omega^2}{\delta} - \frac{\Omega^2}{\delta - \Delta^{(ij)}_{\rm p}}$ and $\bar{\Delta}^{(i)}_{\rm ls} = \frac{\Omega^2}{\delta} - \sum_{j\neq i}\frac{\Omega^2}{\delta - \Delta^{(ij)}_{\rm p}}$ as derived in appendix D.

2.3. Emergence of dark multipartite entangled states for open-system dynamics

The dissipative many-body entanglement for the steady state $\lim_{t\to\infty}\hat{\rho} = \hat{\rho}_{ss}$ is generated as follows. We first identify the spectrum $\{\epsilon_i, |\epsilon_i\rangle\}$ of $\hat{H}_{xy}$ in the $n = 1$ subspace. As shown by figure 1(b), our goal is to set J_{ij}, $\bar{\Delta}^{(i)}_{\rm ls}$ such that one of the eigenstates, say $|\epsilon_1\rangle$, corresponds to a product of W state $|W\rangle_A = \sum_{i\in A}|\tilde{r}^{(1)}_i\rangle$ for a subset A of atoms ('system atoms') and ground state $|g\cdots g\rangle_B$ for another subset B ('reservoir atoms'), thereby leading to $|\epsilon_1\rangle = |W\rangle_A \otimes |g\cdots g\rangle_B$, while all the other eigenstates contain $|r\rangle_B$ for at least one (or more) atom in B. By enhancing $\Gamma_i \to \Gamma$ for atoms B, the net result is that all the eigenstates except $|\epsilon_1\rangle$ become susceptible to a decay to $|\tilde{G}\rangle$, leaving $|\epsilon_1\rangle$ as a unique dark state (i.e., zero-mode eigenstate) of the Lindbladian dynamics. In figure 1(a), we take the two edge atoms at 1 and N as reservoir atoms B, for which we control the relative hopping rates J_{ij} to obtain dark resonance for atoms B so that $|\epsilon_1\rangle$ has vanishing coefficients for $|\tilde{r}^{(1)}_1\rangle$ and $|\tilde{r}^{(1)}_N\rangle$. For a fixed detuning, J_{ij} is purely determined by the relative strength between nearest (a_0) and next-nearest (a_1) neighbor interactions $\xi = a_1/a_0$.

More specifically, the dark resonances $J_{i,i+1} = -J_{i,i+2}$ occur for atoms $\{1, N\}$ at the lattice boundary of a 1D staggered triangular lattice in figure 1(a) for $\xi = \sqrt[6]{3}$ and $N = 4$. More generally, for $N \gg 4$, quantum interference between multiple pathways $|\tilde{r}^{(1)}_i\rangle \leftrightarrow |\tilde{r}^{(1)}_j\rangle$ occurs so that one of the eigenstates of $\hat{H}_{xy}$,$|\epsilon_1\rangle = |W\rangle_A \otimes |g\cdots g\rangle_B$, emerges as the unique dark state (see appendix E). This process is analogous to coherent population trapping for levels consisting of 'radiative' states $\{|\tilde{r}^{(1)}_{i\in B}\rangle\}$ with decay rate $\Gamma_{i\in B} \gg \Gamma_r$ coupled to 'metastable' states $\{|\tilde{r}^{(1)}_{i\in A}\rangle\}$. We thereby define atoms B as reservoir modes, whereby the atoms are continuously projected to the ground state by spontaneous emission Γ in a manner similar to sympathetic cooling [49]. In order to enable this process, we locally enhance the decoherence $\Gamma \simeq 4|\Omega_d|^2/\Gamma_e$ for the reservoir atoms B by $\simeq 10^4$ relative to the radiative rates Γ_r of the system atoms A. Any Rydberg population in atoms B will cause the overall atomic state to become 'bright' and decay until it reaches the unique steady state $|\epsilon_1\rangle$. Many-body entanglement is thereby auto-stabilized for the stationary state $\hat{\rho}_{ss} = |\epsilon_1\rangle\langle\epsilon_1|$ in the presence of noise and decoherence.

In other words, during the entanglement pumping stage, the population is constantly projected to some superposition state $|\epsilon'(t)\rangle$ of eigenstates $\{|\epsilon_\mu\rangle\}$ by the decay channels $n = 2 \to n = 1$ via atoms B. If $|\langle\epsilon_1|\epsilon'(t)\rangle| < 1$, the Rydberg population $|\tilde{r}^{(1)}_i\rangle$ will delocalize until it populates the reservoir atoms, thereby quickly decaying to $|\tilde{G}\rangle$ before being repumped by two-photon transition hamiltonian $\hat{H}_2$. After several cycles of $n = 0 \to n = 2$ (via $\hat{H}_2$) and $n \to n - 1$ (via Γ), the atomic population accumulates into the unique 'dark' eigenstate $|\epsilon_1\rangle$ of $\hat{H}_{xy}$.

Indeed, the entanglement dynamics displays an intricate behavior, as the atomic sample is driven to the steady state $\hat{\rho}_{ss}$. At the early stage of Liouvillian dynamics ($0 \leqslant t_1 \leqslant 1/\Gamma$), atoms in $|\tilde{G}\rangle = |g\cdots g\rangle$ are rapidly pumped to the $n = 1$ subspace. The Rydberg excitation then delocalizes under $\hat{H}_{xy}$ with off-resonant Raman transitions J_{ij}. At the final stage ($t_2 \gg 1/\Gamma$), the Rydberg lattice gas $\hat{\rho}$ is dissipatively pumped to a W-like entangled state $|W\rangle_A$, which separates from $|g\cdots g\rangle_B$. The entanglement fidelity F is thereby determined by the 'branching' ratio $\Gamma_r/\Gamma \simeq 10^{-4}$ between the lifetimes of dissipative and coherent dynamics. Because our procedure does not involve adiabatic evolutions, our dark-state pumping protocol is scalable to arbitrarily large N with sample size extended over $L \sim Na_0/2 \gg d_B$ only limited by $F = 1 - \mathcal{O}(\Gamma_r/\Gamma)$.

3. Results

3.1. Open-system dynamics for bipartite atomic entanglement

In the following, we perform a numerical analysis of the relaxation behavior of the Rydberg gas towards a stationary bipartite entanglement for atom number $N = 4$ and enhanced radiative rates $\Gamma_{1,N} = \Gamma$ for the edge atoms by taking the full Hamiltonian in equation (1). Figure 2(a) displays the contour map of entanglement fidelity $F_2 = {}_A\langle\psi_2|\,{\rm Tr}_B[\hat{\rho}_{\rm ss}]\,|\psi_2\rangle_A$, for the stationary state $\hat{\rho}_{\rm ss}$ and the target state $|\psi_2\rangle_A = \frac{1}{\sqrt{2}}(|g_2r_3\rangle + |r_2g_3\rangle)_A$, as a function of interaction parameter ξ and distance a_0 (in units of blockade radius $d_B = \sqrt[6]{C_6/w_d}$). The profile of fidelity along a_0 depicts the requirement of Rydberg blockade regime $a_0 < d_B$ to provide sufficient nonlinearity in n (figure 1(b)) for selectively driving transitions $|\tilde{G}\rangle \leftrightarrow |\tilde{r}^{(2)}_{i,i+1}\rangle$ and adiabatically eliminating subspaces $n = 0, 2$ (appendix D). Atoms in the region $0.2 \leqslant a_0/d_B \leqslant 0.5$ are thereby efficiently pumped to the single-excitation subspace. The interaction parameter ξ is tuned to numerically maximize the steady-state entanglement fidelity up to $F_2 = 0.9982$ for $\xi_1 = \sqrt[6]{3}$ and $\xi_2 = 0.36$ at $a_0/d_B = 0.26$. To validate our

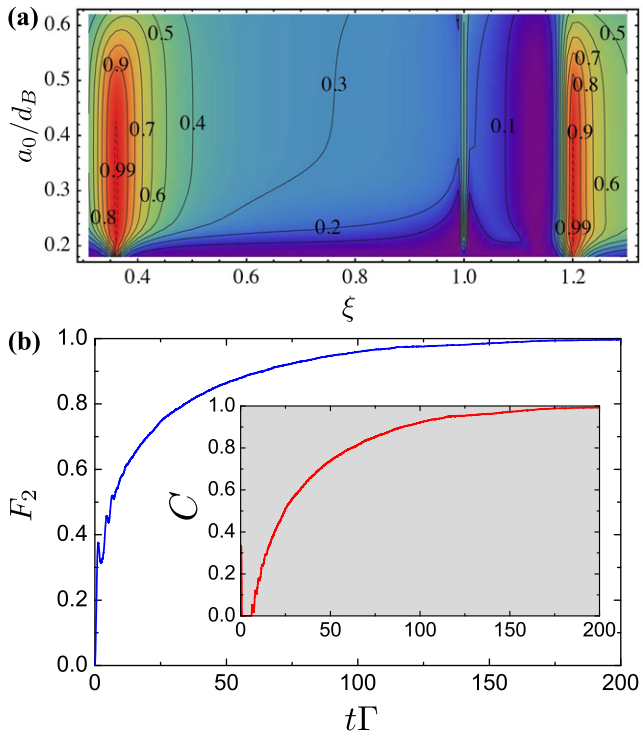

Figure 2. Driven-dissipative dynamics of bipartite atomic entanglement. (a) Contour of stationary entanglement fidelity F_2 with interaction parameter ξ and distance a_0 (in units of blockade radius d_B). (b) Dynamics of entanglement fidelity $F_2(t)$ as a function of pumping time (in units of Γ). Inset. Temporal evolution of concurrence C from unentangled $C = 0$ to maximal entanglement $C = 1$ for the parameters: $\delta = w_d/2(a_0/d_B)^6, \Omega = 10^3\Gamma$, and $\Gamma_{1,4} = 10^4\Gamma_r$ for atoms 1, 4 with $\{\xi, a_0/d_B\} = \{\sqrt[6]{3}, 0.26\}$.

entanglement pumping scheme, we further show the dissipative dynamics of concurrence C at ξ_1 in the inset of figure 2(b). The atomic sample is driven to a maximally entangled state with $F_2 = 0.9965$ within $t\Gamma = 200$.

3.2. Evolution of many-body entanglement and uncertainty-based entanglement witness

Now, let us treat the case of many-body entanglement with $N = 6$ atoms in the 1D lattice with equation (1) as an example of multipartite system. With same parameter set Ω and Γ, we simulate the dissipative dynamics of entanglement fidelity $F_4(t) = {}_A\langle\psi_4|\ \mathrm{Tr}_B[\hat{\rho}(t)]\ |\psi_4\rangle_A$ with respect to the ideal symmetric W state $|\psi_4\rangle_A = \frac{1}{2}\sum_{i=2}^{5}|\tilde{r}_i^{(1)}\rangle_A$ by way of quantum-trajectory method (see figure 3(a)). Here, we have optimized the steady-state fidelity $\max(F_4) = 0.9912$ for the parameters $\{\xi, a_0/d_B\} = \{1.1996, 0.285\}$, thereby setting a symmetric quadripartite W-state $|\epsilon_1\rangle = |\psi_4\rangle_A \otimes |g_1 g_6\rangle_B$ as the dark state.

The transitions of many-body entanglement under dissipative dynamics are detected by the uncertainty relations [46–48], which serves as the collective entanglement witness $\{\Delta(t), \gamma_c(t)\}$ [1]. The uncertainty $\Delta = \sum_i\langle\delta^2\hat{\Pi}_i\rangle$ measures the total variance of projection operators $\hat{\Pi}_i = |W_i\rangle\langle W_i|$ to N_A-dimensional W-state basis $|W_i\rangle$, while $\gamma_c = \frac{2N_A}{N_A-1}\frac{p_{\geqslant 2}p_0}{p_1^2}$ detects the amount of higher-order spin-waves (e.g., $p_2 = \sum_{i\neq j}\langle\hat{\sigma}_{rr}^{(i)}\hat{\sigma}_{rr}^{(j)}\rangle$)and ground-state fraction $p_0 = \sum_i\langle\hat{\sigma}_{gg}^{(i)}\rangle$ relative to the singly excited spin wave $p_1 = \sum_i\langle\hat{\sigma}_{rr}^{(i)}\rangle$, where N_A is the number of atoms in A. For an ideal W-state, $\min\{\Delta, \gamma_c\} \to \{0, 0\}$, while the boundary $\Delta_b^{(k-1)}$ represents the minimum uncertainty for $(k-1)$-partite entangled states for a given γ_c. Violation of the uncertainty bound $\Delta(\hat{\rho}) < \Delta_b^{(k-1)}$ then signals the presence of genuine k-partite entanglement stored in $\hat{\rho}(t)$, with the full N_A-partite entanglement certified by $0 \leqslant \Delta(\hat{\rho}) < \Delta_b^{(N_A-1)}$.

Experimentally, the entanglement witness $\{\Delta(\hat{\rho}), \gamma_c(\hat{\rho})\}$ can be determined by detecting the fluctuation $\delta^2\vec{\mathcal{S}}_t$ in the collective transverse spin component $\vec{\mathcal{S}}_t = \sum_i\{\cos\theta_d\hat{\sigma}_x^{(i)}, \sin\theta_d\hat{\sigma}_y^{(i)}\}$ and the excitation statistics $\{p_0, p_1, p_{\geqslant 2}\}$, where θ_d is the detection angle in the transverse plane $x-y$. As discussed in [48], $\Delta(\hat{\rho}) \leqslant \tilde{\Delta}(\hat{\rho}) = \left(\frac{N-1}{N}\right) \times (1 - N^2\tilde{d}^2)$, where $\tilde{d} = \frac{2}{N(N-1)}\sum_{ij}|d_{ij}|$ is the average off-diagonal coherence $d_{ij} = |g\rangle_i\langle r| \otimes |r\rangle_j\langle g|$ for the reduced density matrix $\hat{\rho}_1$ in the single-excitation subspace. Since $\min\langle\delta^2\mathcal{S}_t\rangle_{\theta_d} = 2\sum_{ij}|d_{ij}|$, we find the following upper bound of the measured variance $\tilde{\Delta}(\hat{\rho}) = \frac{N}{N-1} \times [1 - \left(\frac{\min\langle\delta^2\mathcal{S}_t\rangle_{\theta_d}}{N-1}\right)^2]$. The quantum statistics $\gamma_c = \left(\frac{2N}{N-1}\right)\frac{p_{\geqslant 2}p_0}{p_1^2}$ can be detected by the total

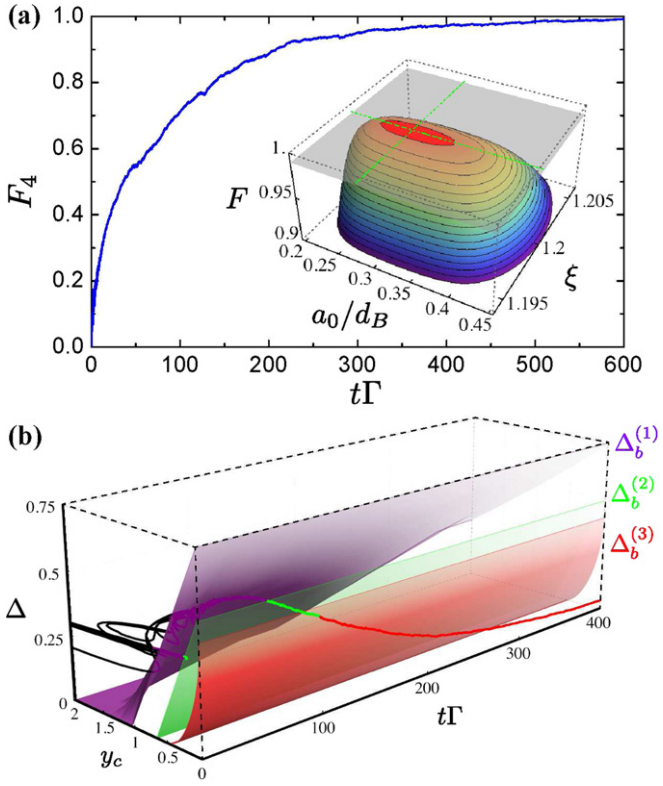

Figure 3. Driven-dissipative dynamics of many-body entanglement for six atoms. (a) Dynamics of entanglement fidelity F_4 at maximum point $\{\xi,\ a_0/d_B\} = \{1.1996,\ 0.285\}$ simulated by way of Monte Carlo wavefunction (averaged over 500 trajectories). Inset. 3D map of steady-state entanglement fidelity F_4 for interaction parameter ξ and distance a_0 (in units of blockade radius d_B). $F_4 > 0.99$ for $0.25 \leqslant a_0 \leqslant 0.35$ (b) Dissipative preparation of genuine quadripartite entangled state. The entanglement parameters $\{\Delta(\rho),\ y_c\}$ transit from fully separable (black line) to bipartite entanglement (purple line, $t_2\Gamma \simeq 2$), to tripartite entanglement (green line, $t_3\Gamma \simeq 65$), and to stationary quadripartite entanglement (red line, $t_4\Gamma \simeq 100$). The colored surfaces represent the minimum uncertainties Δ for fully separable states (purple), and for states containing bipartite (green) and tripartite entanglement (red) for a given y_c.

excitation statistics $\{p_0,\ p_1,\ p_{\geqslant 2}\}$ with MCP ionization signals. Hence, our entanglement witness can be readily implemented even for *low-resolution* Rydberg experiments without the capability to locally detect the state of single atoms in the lattice.

By applying the witness $\{\Delta,\ y_c\}$, we observe that atoms initially in ground state are dissipatively driven to the quadripartite entangled W state by sequentially crossing the boundaries $\Delta_b^{(1)}$, $\Delta_b^{(2)}$, $\Delta_b^{(3)}$ in figure 3(b), thereby progressing towards the steady-state with $F_4 > 0.99$. The transitions of entanglement depth k are indicated by black, purple, green, and red lines of figure 3(b) for the average trajectory $\hat{\rho}(t)$. For pumping time $t_4 \sim 100/\Gamma$, the many-body system exhibits a full quadripartite entanglement with a moderate atom number $N = 6$, and reach $\{\Delta,\ y_c\}|_{ss} \rightarrow \{1.5 \times 10^{-2},\ 2 \times 10^{-4}\}$, as the atoms are pumped to the desired eigenstate $|\epsilon_1\rangle$. In the appendix E, we also discuss our numerical result for the formation of stationary hexapartite entanglement for $N = 10$ atoms with $F_6 > 0.99$ (see figure E2).

3.3. Finite-size scaling of steady-state entanglement

Next, we move on to the question of finite-size scaling behavior of the stationary many-body entanglement. Although the full dynamical simulation for large N is beyond our computational capability, the steady-state entanglement can be established by analyzing the unique eigenstate $|\epsilon_1\rangle$ that meets the dark resonance condition $\xi = \xi_1$, for which $J_{i,i+1} = -J_{i,i+2}$. Perturbations by higher-order interactions are negligible, as $\sum_{x>2}^{\infty}|J_{i,i+x}|/|J_{i,i+1}| \ll 10^{-2}$. We truncate our analysis up to next-nearest-neighbor interactions for the following discussion. We define the entanglement depth k in accord with the concept of k-producibility for qubits [1, 42], thereby identifying the minimal depth for genuine k_m-partite entanglement to produce the purported state $\hat{\rho}_{ss}$ (for details, see appendix E).

We directly diagonalize the many-body Hamiltonian $\hat{H}_{xy}$ for ξ_1, and characterize the resulting entanglement depth k of the stationary eigenstate $|\epsilon_1\rangle$ up to $N \rightarrow 128$. Figure 4 captures our result of $\{\Delta,\ y_c \rightarrow 0\}$ for the dark state $|\epsilon_1\rangle = |W_k\rangle_A \otimes |g\cdots g\rangle_B$, where $|W_k\rangle_A$ is the k-partite symmetric W state. Due to the nonlinear sensitivity of our witness for some region k, we characterize the scaling of the *minimal* entanglement depth $k_m \leqslant k$. The

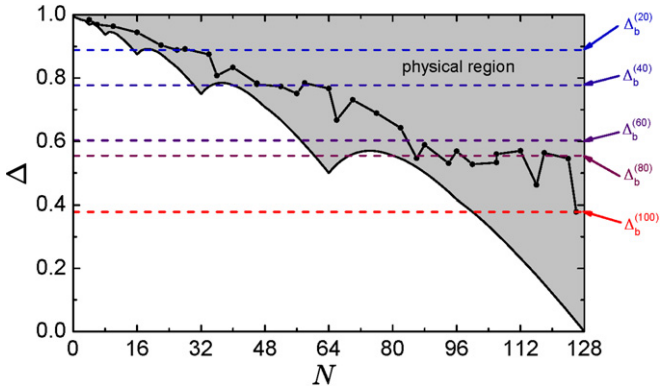

Figure 4. Finite-size scaling behavior of many-body entanglement depth. Multipartite entanglement behavior of the many-body system $\hat{\rho}_{ss}$ is probed with quantum uncertainty witness Δ for $\gamma_c \to 0$ by way of direct diagonalization of $\hat{H}_{xy}$ as a function of atom number N. We obtain stationary eigenstates $\hat{\rho}_{ss} = |\epsilon_1\rangle\langle\epsilon_1|$, exhibiting up to hectapartite entanglement for $N = 126$ atoms. The shaded area refers to the physical region formed by convex combination of all pure and mixed states for a given N, thereby representing the state space for which entanglement depth k can be defined with $k \leqslant N$. The uncertainty boundaries for 20-partite, 40-partite, 60-partite, 80-partite, 100-partite entanglement are shown as dashed lines.

shaded area represents the physical region, whereby k_m-partite entanglement could be defined for a given N, and the dashed lines are the uncertainty bounds for $0 \sim 100$-partite entanglement (with 20-partite increments). Remarkably, we observe a favorable scaling up to genuine 'hectapartite' ($k_m = 100$) entanglement for $N = 126$ atoms.

4. Experimental feasibility

Our entanglement pumping scheme is experimentally feasible. By exciting ^{85}Rb atoms to Rydberg state $|r\rangle = |100S_{1/2}\rangle$ with local mixing of decohering state $|e\rangle = |5P_{1/2}\rangle$, quadripartite entangled states could be prepared for $F_4 \geqslant 0.99$ within the pumping time $t_p = 60\ \mu$s in the region $1.9(2.3)\ \mu\text{m} \leqslant a_0(a_1) \leqslant 2.1(2.5)\ \mu$m with parameters $C_6 = 56$ THz μm^6, $\Gamma_r \simeq 1$ kHz, $\Gamma = 10$ MHz, and with driving fields $\Omega = 1$ GHz in the far-off resonant limit $\delta \simeq 400$ GHz (effective Rabi frequency $\sim$10 MHz), and $d_B = 5.8\ \mu$m [50–53]. The limit for any driven-dissipative approach with Rydberg lattice gases will be the photoionization lifetime $t_\pi \gg 10$ ms for the given Ω [54], thereby $t_p \ll t_\pi$. Instead, if we reduce the fidelity threshold $F_4 \to 0.9$ ($\Gamma_r/\Gamma = 10^{-3}$), the steady state can be achieved within $t_p = 600\ \mu\text{s} \ll 1\text{s} \ll t_\pi$ for relaxed parameters $\Gamma = 1$ MHz, $\Omega = 50$ MHz, and $d_B = 9.6\ \mu$m over the region of $3.8(4.5)\ \mu\text{m} \leqslant a_0(a_1) \leqslant 3.9(4.7)\ \mu$m. In appendix G, we have discussed a wide range of experimental parameters with Rb and Cs, including direct UV excitation to $|r\rangle = |nP_{3/2}\rangle$ state with $|e\rangle = |7S_{1/2}\rangle$, which offers lower $\Gamma_r \to 300$ Hz and thereby improved fidelity $F \sim 1 - \mathcal{O}(\Gamma_r/\Gamma)$ for fixed Ω, Γ [55]. For example, with $|r\rangle = |100P_{3/2}\rangle$, we expect to obtain high fidelity $F_4 > 0.99$ with moderate driving field $\Omega = 50$ MHz and lattice constants $(a_0,\ a_1) \sim 3\ \mu$m.

In our driven-dissipative protocol, the dark state is selected by optimizing the set of parameters for the lattice constants $(a_0,\ a_1)$ in the limits of (i) strong saturation $(\Omega/\Gamma_r,\ \Omega^2/\delta\Gamma_r) \gg 1$ and (ii) local dissipation $\Gamma/\Gamma_r \gg 1$. Indeed, within the single-excitation subspace, the parameters $(a_0,\ a_1)$ determines the full spectrum of the XY spin Hamiltonian H_{xy}, thereby setting the conditions for dark-state engineering (appendix E). By virtue of locally enhanced decoherence for edge atoms, we then isolate a single eigenstate $|\epsilon_1\rangle$, as the unique dark state. As shown in figures 2 and 3, our method can stabilize high-fidelity steady-state entanglement over a wide range of lattice parameters (see also appendix G for the experimental parameters).

One crucial benefit of our method for quantum-reservoir engineering is that the dark state $|\epsilon_1\rangle$ is stabilized by many-body interactions and local decoherence, and that it offers built-in error-correcting features and robustness against variation in the driving fields and decay rates. This prediction is supported by the wide range of laboratory parameters (over many orders of magnitude) in tables G1 and G2, which allow high-fidelity entanglement. Experimentally, the lattice parameters $(a_0,\ a_1)$ can be coarse-tuned by locally monitoring the flourescence for the edge atoms. When the dark state is fully populated, the successful passage into the steady state may be confirmed by the observation of inhibited atomic scattering.

The bottleneck for any driven-dissipation protocol is the relaxation time scale t_p to reach the desired steady state. As further discussed in appendix G, the quantum jumps in the $n = 1$ subspace occur in a characteristic time $\sim\mathcal{O}(N^2)$ due to the time scale for the quantum walk of $|\tilde{r}_i^{(1)}\rangle$ to reach the 'reservoir' atoms at the edge. On the other hand, if we were to address every 'zeros' for the dark state equations (E.5) and (E.6) in appendix E) by

Ω_d with $N_{\rm res} > 2$ reservoir atoms, the pumping time $t_{\rm p} \sim \mathcal{O}(N_{\rm sys})$ scales linear to the number $N_{\rm sys}$ of eigenstates $\{|\epsilon_\mu\rangle\}$ within the single-excitation subspace, where $N_{\rm sys}$ is the number of system atoms. The relaxation time for figures 2 and 3 and E2 is consistent with the scaling $t_{\rm p} \sim \mathcal{O}(N_{\rm sys})$. As discussed in appendix G, our method can be applied to generate stationary hectapartite entanglement within $t_{\rm p} \simeq 10$ ms $\ll t_\pi$ for $N = 126$ atoms with optically accessible $(a_0,\ a_1) > 1$ μm, where t_π is the photo-ionization time. Compared to direct adiabatic passage with time-varying fields [36, 37], the range of entanglement $L \simeq Na_0/2 = 63$ μm surpasses the blockade radius $d_B = 9.6$ μm by more than six fold, testifying the intrinsic scalability of our method with engineered driven-dissipation.

In terms of the initialization of the atoms in the 1D lattice, the atoms would need to be confined in each well with unit filling factor. In practice, such a low entropy state could be achieved by the superfluid-Mott insulator transition or by the manipulation of laser-induced atomic collisions with blue-detuned potentials [56]. The 1D staggered triangular lattice can be realized in a free-space superlattice configuration [57]. Since the general principle of our protocol is not necessarily confined to a particular lattice configuration, one could explore other configurations in 1D and 2D with arbitrary trap potential landscapes created by spatial light modulators in [58].

Alternatively, it is possible to load a mesoscopic number of atoms N_i at each lattice site with weak optical confinement perpendicular to the lattice plane [57], and use the effective spin-1/2 degree of freedom under collective Rydberg blockade [22]. This may be particularly crucial for realistic experimental settings, where the collectively enhanced Rabi frequency $\Omega^{(N)} = \sqrt{N}_i\Omega$ can be used to circumvent the small single-photon Rabi frequency with limited optical power. The effect of the finite atomic wavepackets in the potential landscape is negligible with the steady-state entanglement fidelity bounded by $F > 1 - \mathcal{O}(\delta\Delta_{\rm p}/\Delta_{\rm p})$, in which $F > 0.95$ for the typical values of zero-point fluctuation of atoms in dipole traps (appendix G). Our method does not rely on the dynamics of coherent delocalization and Anderson localization for disorded spin arrays is not a relevant phenomena for the relaxation to steady-state entanglement.

For $N \gg 126$, atoms can be embedded in photonic crystal waveguides to mediate effective atom-atom interactions. Dispersive optical interactions near band edges can induce dipole–dipole oscillations $\hat{H}_{xy}$ and 'Rydberg' blockades $\hat{H}_2$ with tailored scaling $\Delta_{\rm p}^{(ij)} \sim c^{-x_{ij}}$ between low-lying excited atoms [59, 60]. Decay rates $\Gamma_i = \Gamma'$ can be controlled by the density of states [61].

5. Conclusion

We have examined the conditions under which driven-dissipative dynamics displays a rich family of many-body entangled states, and have provided a criteria for the purported entanglement. By way of engineered driven-dissipation, genuine multipartite entangled states can be prepared efficiently as steady states of the dissipative time evolution through continuous optical driving from arbitrary initiate states, and the stationary entanglement shows a favorable long-range behavior up to entanglement depth $k_m = 100$ for $N = 126$ atoms. In comparison to other work with coherent Rydberg excitation, our method allows the deterministic production of many-body entangled states over length scales unlimited by the blockade radius. More generally, the delocalization dynamics for our lattice Hamiltonian $\hat{H}_{xy}$ in the high-order subspace n (see appendix B) can be extended to examine locality estimates of many-body systems [62–64] and bosonic sampling for quantum algorithms [65]. Massively entangled W states with $N \gg 2$ stabilized by engineered driven-dissipation may be applied for 'all-versus-nothing' tests of extreme nonlocality [66]. Our work paves the way for the stabilization of exotic entangled states with an open many-body system enabled by well-controlled Rydberg-mediated laser interactions and local decoherence [1–3], as well as for the advanced protocols with dissipative quantum computing and reservoir engineering.

Note: A related proposal for stationary many-body entanglement has been presented recently in [67] with resonant dipole–dipole interactions (RDDIs) between two Rydberg ensembles. In [68], our work has been generalized to the stabilization of arbitrary many-body states in a system-independent manner.

Acknowledgments

We gratefully acknowledge the discussions with HJ Kimble, P Lougovski, K Mølmer, and P Zoller. This work is funded by NSERC through the Discovery and RTI Programs, Ontario Ministry of Research & Innovation, Industry Canada, and KIST Institutional Program (Prog. No. 2V04280). We acknowledge the support of NVIDIA Corporation with equipment donations.

Appendix A. Control of spontaneous emission rates

As discussed in the main text, for reservoir sites $i \in B$, atoms initially in the Rydberg state $|r\rangle$ with decay rate Γ_r radiatively couple to a highly decohering state $|e\rangle$ with decay rate $\Gamma_e \gg \Gamma_r$ so that atoms in bipartition B can behave as an effective 'reservoir' channel for the 'system' atoms in partition A. In this section, we discuss how we could manipulate the spontaneous emission rate Γ_i of the Rydberg state $|r\rangle$ for the 'reservoir' atoms.

As illustrated in figure 1(a), we consider a Λ-type energy level diagram, where $|r\rangle$ is dressed with $|e\rangle$ by auxiliary field with Rabi frequency Ω_d. In the rotating-wave frame of the dressing laser, the Hamiltonian is given by

$$\hat{H}_d = \Delta_d \hat{\sigma}_{ee}^{(i)} + \Omega_d\left(\hat{\sigma}_{er}^{(i)} + \hat{\sigma}_{re}^{(i)}\right). \tag{A.1}$$

The resulting optical Bloch equations are, then

$$\dot{\sigma}_{ge}^{(i)} = -\gamma_e \sigma_{ge}^{(i)} + \mathrm{i}\Delta_d \sigma_{ge}^{(i)} + \mathrm{i}\Omega_d \sigma_{gr}^{(i)}, \tag{A.2}$$

$$\dot{\sigma}_{gr}^{(i)} = -\gamma_r \sigma_{gr}^{(i)} + \mathrm{i}\Omega_d \sigma_{ge}^{(i)}, \tag{A.3}$$

where $\gamma_{e,r} = \Gamma_{e,r}/2$ and Δ_d is the detuning for the dressing field Ω_d relative to the transition $|e\rangle \leftrightarrow |r\rangle$. In writing equations (A.2) and (A.3), we have neglected the Langevin noise forces $\hat{F}_{\mu\nu}$ and assumed c-number counterparts for $\hat{\sigma}_{\mu\nu}^{(i)} \mapsto \sigma_{\mu\nu}^{(i)}$. Hence, we find that the atomic coherence $\sigma_{gr}^{(i)}(t)$ between $|g\rangle$, $|r\rangle$ obeys the following equation of motion

$$\ddot{\tilde{\sigma}}_{gr}^{(i)} - \left(\mathrm{i}\tilde{\Delta} + \gamma_r\right)\dot{\tilde{\sigma}}_{gr}^{(i)} \mathrm{e}^{\left(-\mathrm{i}\tilde{\Delta}-\gamma_r\right)t} + \Omega_d^2 \tilde{\sigma}_{gr}^{(i)} \mathrm{e}^{\left(-\mathrm{i}\tilde{\Delta}-\gamma_r\right)t} = 0, \tag{A.4}$$

with $\tilde{\sigma}_{gr}^{(i)} = \sigma_{gr}^{(i)} \mathrm{e}^{-\gamma_r t}$ and $\tilde{\Delta} = \mathrm{i}\gamma_e + \Delta_d$.

Figure A1 shows the dynamics of Rydberg population $\sigma_{rr}^{(i)}(t) = \sigma_{rg}^{(i)}\sigma_{gr}^{(i)}$ obtained by numerically solving equations (A.2) and (A.3) for the parameters of figures 2–4 with $\Gamma_e = 10^4\Gamma_r$. The black solid (dashed) line is the atomic dynamics for $\Omega_d = 10\Gamma_r$ ($\Omega_d \in \{10^2\Gamma_r, \ldots, 9 \times 10^2\Gamma_r\}$ with $10^2\Gamma_r$ increments). The red line is the result of atomic decay $\Gamma \simeq 10^3\Gamma_r$ with $\Omega_d = 10^3\Gamma_r$. As we increase $\Omega_d \to \Gamma_e$, we find that the effective decay rate for the reservoir atoms scales with $\Gamma \sim 4|\Omega_d|^2/\Gamma_e$ up to $\Omega_d \sim 0.1\Gamma_e$.

In order to understand the dynamics, we formally integrate equation (A.2) to obtain $\sigma_{ge}^{(i)} \mathrm{e}^{-\mathrm{i}\tilde{\Delta}t} = \mathrm{i}\Omega_d \int \sigma_{gr}^{(i)} \mathrm{e}^{-\mathrm{i}\tilde{\Delta}t} \mathrm{d}t \simeq \dfrac{\Omega_d}{\tilde{\Delta}} \sigma_{gr}^{(i)} \mathrm{e}^{-\mathrm{i}\tilde{\Delta}t}$. Assuming slowly varying amplitude $\dot{\sigma}_{gr}^{(i)}$ for $\Omega_d \ll \gamma_e$, we obtain the following equation of motion

$$\dot{\sigma}_{gr}^{(i)} = -\left(\gamma_r + \frac{\mathrm{i}\Omega_d^2}{\tilde{\Delta}}\right)\sigma_{gr}^{(i)}, \tag{A.5}$$

where the effective decay rate is given by $\gamma_{\mathrm{eff}} = \gamma_r + \dfrac{\gamma_e |\Omega_d|^2}{|\Delta|^2 + \gamma_e^2}$ with $\Gamma = 2\gamma_{\mathrm{eff}}$. As further discussed below, $|r\rangle = |100S_{1/2}\rangle$ and $|e\rangle = |5P_{1/2}\rangle$ have decay rates with $\Gamma_e/\Gamma_r \simeq 10^4$. Hence, decay rates for reservoir sites could be enhanced up to 4 order of magnitude with $\Gamma/\Gamma_r \to 10^4$.

Appendix B. Optical pumping to arbitrary n-subspace in an anharmonic Rydberg ladder

Now, let us discuss the possibility of optically pumping the system $\hat{\rho}$ of N atoms to an arbitrary target n_t-excitation subspace with $n_t < N - 2$, for which $n_t = 1$ in the main text. This is achieved by a set of n_t lasers resonantly driving the two-photon transitions $n \to n + 2$ ($n \in \{0, \ldots, n_t - 1\}$) with effective Rabi frequencies $\Omega_2^{(n)}$ (see figure B1 (a)) and the three-photon transition $n_t - 2 \to n_t + 1$ with effective Rabi frequency $\Omega_3^{(n)}$ (see figure B1(b)). Because $\mathcal{L}\hat{\rho}$ dissipates the levels $n \to n - 1$, the atomic population is pumped to the target subspace n_t (see figure B1(b)). For the case of $n_t = 1$, $\Omega_2^{(0)}$ is provided by a single global field Ω for the entire atoms (see figure B1(c)).

The efficacy of this procedure to address only a particular transition $n \to n'$ depends on the anharmonicity in the Rydberg spectrum $V_n = \langle n|\ \hat{V}_{\mathrm{p}}\ |n\rangle$, where $\hat{V}_{\mathrm{p}} = \sum_{\langle i,j\rangle}^{N} \Delta_{\mathrm{p}}^{(ij)} \hat{\sigma}_{rr}^{(i)} \hat{\sigma}_{rr}^{(j)}$ and $|n\rangle$ represents the most shifted state of the n subspace. The V_n is obtained by degenerate Rydberg configurations with n-nearest neighbor excitations (e.g., $|n\rangle = |r_1, \ldots, r_n, g_{n+1}, \ldots, g_N\rangle$). The Rydberg spectrum is then given by

$$V_n = \sum_{i=1}^{n-1} \sum_{j=i+1}^{n} \Delta_{\mathrm{p}}^{(ij)}. \tag{B.1}$$

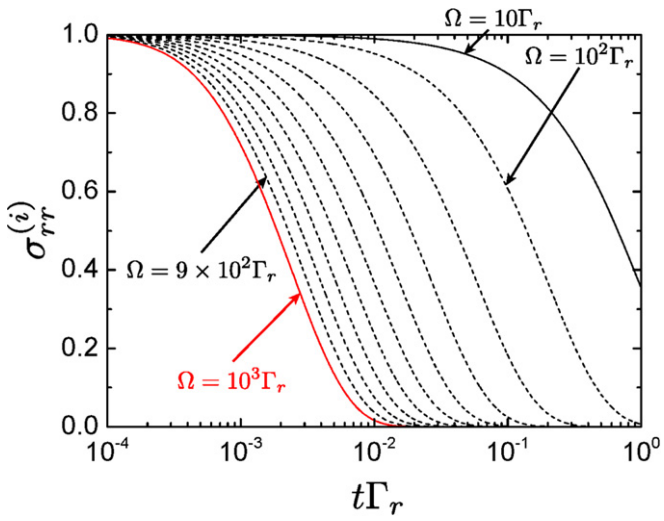

Figure A1. Enhancement in the decay rate $\gamma_{\rm eff} \simeq |\Omega_d|^2/\Gamma_e$ as a function of the strength of dressing field Ω_d. The parameters are $\Gamma_e = 10^4\Gamma_r$, and resonant dressing $\Delta_d = 0$.

The transition energy for $n \to n+2$ is then

$$V_{n+2} - V_n = 2\sum_{i=1}^{n} \Delta_{\rm p}^{(i,n+1)} + \Delta_{\rm p}^{(1,n+2)}, \tag{B.2}$$

so that the anharmonicity is given by

$$\delta V_{n+2,n} = \Delta_{\rm p}^{(1,n+1)} + \Delta_{\rm p}^{(1,n+2)}. \tag{B.3}$$

As shown in figure B1(b), for a given target subspace n_t, we terminate the two-photon excitations to $n_t - 1 \to n_t + 1$. All subspaces with $n \in \{0, \ldots, n_t - 1, n_t + 1\}$ are resonantly connected by two-photon transitions $\Omega_2^{(n)}$ with detunings $\delta_n^{(2)} = (V_{n+2} - V_n)/2$ and by three-photon Ω_3 coupling with detuning $\delta_{n_t-2}^{(3)} = (V_{n_t+1} - V_{n_t-2})/3$, except for the n_t subspace (see figure B1(b)). The Rydberg blockade condition for the two-photon transition $n \to n+2$ is then given by

$$\delta V_{n+2,n} > w_d^{(2)}, \tag{B.4}$$

where $w_d^{(2)} = \sqrt{\Gamma_r^2 + 2|\Omega_2^{(n)}|^2}$ is the 'two-photon' power-broadened width of the transition $n \to n+2$ and $\Omega_2^{(n)} = 2\Omega^2/\delta_n^{(2)}$ is the effective Rabi frequency. Critically, $w_d^{(2)} \sim 2\sqrt{2}\,\Omega^2/\delta_n^{(2)} \ll w_d$, so that the higher-order two-photon excitations (e.g., $n = 1 \to n = 3$) can be blocked even for extended samples $L \gg d_B$.

Appendix C. Feasibility of pumping to single-excitation subspace with large N

For $n_t = 1$, by driving the two-photon transition $n = 0 \to n = 2$ with $\delta_0^{(2)} = (V_2 - V_0)/2 = \Delta_{\rm p}^{(1,2)}/2$, the atoms are pumped to a decoherence-free subspace (DFS) for atoms A of the $n_t = 1$ subspace (see figure 2(d)). As discussed in the main text, the DFS is defined by the space spanned by superpositions of $\{|\tilde{r}_{i\in A}^{(1)}\rangle\}$, and the subspace is set for the reservoir atoms B. In this case, high pumping efficiency to $n_t = 1$ is assured if the higher-order transition $n = 1 \to n = 3$ is blockaded for the least shifted state $|r_1, r_2, g_3, \ldots, g_{N-1}, r_N\rangle$ of $n = 3$ subspace, thereby $\Delta_{\rm p}^{(1,N-1)} + \Delta_{\rm p}^{(2,N-1)} > w_d^{(2)}$. For the 1D lattice in figure 1(a), our dissipative pumping scheme works in the region $a_0/d_B \simeq 0.1$ even for $N = 126$ in the extended sample regime $L \gg d_B$, where we take $\Omega = 50\Gamma$, $\Gamma/\Gamma_r = 10^3$ and $\xi = a_1/a_0 \simeq \sqrt[6]{3}$. For the case of Rb with $|r\rangle = |100S_{1/2}\rangle$, the blockade distance is $d_B = 9.6\ \mu$m $\ll L = 63\ \mu$m, so that $(a_0,\ a_1) \simeq (900,\ 1000$ nm).

Appendix D. Derivation of effective spin Hamiltonian

In the off-resonant limit $|\delta - \Delta_{\rm p}^{(ij)}| \gg w_d$, we obtain the effective Hamiltonian $\hat{H}_{\rm eff}$ (equation (2)) by truncating the perturbative expansion to the second order and by time-averaging highly oscillating terms [69],

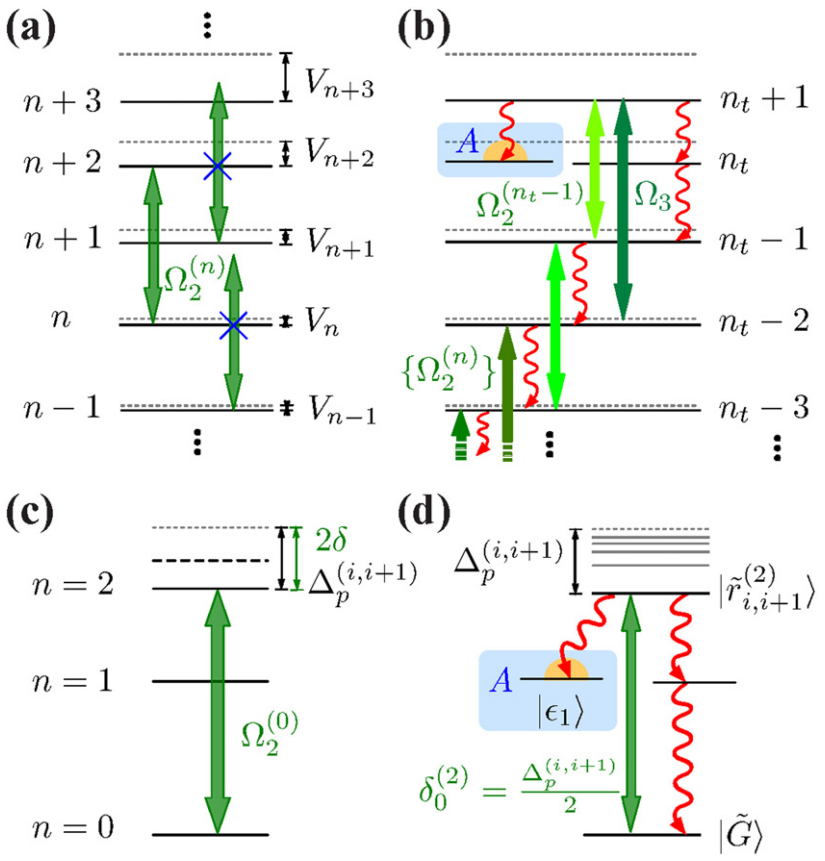

Figure B1. (a) Anharmonic Rydberg spectrum for two-photon transition $\Omega_2^{(n)}$. Dotted (solid) line represents the energy level for non-interacting atoms (the most shifted energy level with Rydberg interaction). (b) A set of $n_t - 1$ two-photon transitions $n \to n+2$ (with $n \in \{0, \ldots, n_t - 1\}$) are resonantly driven at Rabi frequencies $\{\Omega_2^{(n)}\}$, in tandem with a three-photon laser Ω_3 for $n_t - 2 \to n_t + 1$ are required to pump atoms to the target subspace n_t. Non-coupled subspace A of n excitations remains dark throughout the entire driving processes. The target eigenstate is $|\epsilon_1\rangle = \sum_{\{p_i\}\in A} \alpha_{\{p_i\},1} |\tilde{r}_{\{p_i\}}^{(n)}\rangle_A \otimes |g\cdots g\rangle_B$. (c) A single laser is required to drive $n = 0 \to n = 2$ for target subspace $n_t = 1$, (d) For $\delta = \delta_0^{(2)}$, atoms are pumped to the target eigenstate $|\epsilon_1\rangle = \sum_{i\in A} \alpha_{i,1} |\tilde{r}_i^{(1)}\rangle_A \otimes |g\cdots g\rangle_B$, whereby decoherence is enhanced for atoms B.

$$\hat{H}_{\rm eff} = \sum_{m,n} \frac{\left[\hat{h}_m^\dagger, \hat{h}_m\right]}{\bar{\omega}_{mn}} e^{i(\omega_m - \omega_n)t} + \sum_{m,n} \left(\frac{\hat{h}_n \hat{h}_m e^{-i(\omega_m+\omega_n)t}}{\bar{\omega}'_{mn}} + \text{h.c.} \right), \tag{D.1}$$

with the interaction Hamiltonian given by $\hat{H}_{\rm I} = \sum_{n=1} \hat{h}_n e^{-i\omega_n t} + \hat{h}_n^\dagger e^{i\omega_n t}$, where $H_I = e^{iH_0 t} H_1 e^{-iH_0 t}$, $\bar{\omega}_{mn} = [(1/2)(1/\omega_m + 1/\omega_n)]^{-1}$, $\bar{\omega}'_{mn} = [(1/2)(1/\omega_m - 1/\omega_n)]^{-1}$, and ω_n is the detuning between the laser frequency and the Rydberg-shifted transition. In particular, we use $\hat{H} = \hat{H}_0 + \hat{H}_{\rm I}$ with

$$\hat{H}_0 = \sum_{i=1}^{N} \delta \hat{\sigma}_{rr}^{(i)} - \sum_{i<j}^{N} \Delta_{\rm p}^{(ij)} \hat{\sigma}_{rr}^{(i)} \hat{\sigma}_{rr}^{(j)}, \tag{D.2}$$

$$\hat{H}_{\rm I} = \Omega \sum_{i=1}^{N} \left(\hat{\sigma}_{rg}^{(i)} + \hat{\sigma}_{gr}^{(i)} \right), \tag{D.3}$$

with $\hat{\sigma}_{\mu\nu}^{(i)} = |\mu\rangle_i \langle\nu|$ for $\mu, \nu \in \{g, r\}$ and blockade shift $\Delta_{\rm p}^{(ij)} = C_{\rm p} |\vec{x}_i - \vec{x}_j|^{-p}$.

We obtain the following effective Hamiltonian

$$\hat{H}_{xy} = -\sum_{i=1} \bar{\Delta}_{\rm ls}^{(i)} \hat{\sigma}_{rr}^{(i)} + \sum_{i<j} J_{ij} \left(\hat{\sigma}_+^{(i)} \hat{\sigma}_-^{(j)} + \text{h.c.} \right), \tag{D.4}$$

which corresponds to a XY model $\hat{H}_{xy}$ with spin–spin interaction J_{ij} and magnetic field $\Delta_{\rm ls}^{(i)}$, thereby $\hat{H}_{\rm eff} = \hat{H}_{xy}$. After the population is pumped to the n_t subspace (see figure B1(b)), the coherent atomic dynamics is governed by H_{xy} within the n_t subspace.

For $n_t = 1$, the necessary Raman couplings (J_{ij}) and light shifts ($\Delta_{\rm ls}^{(i)}$) are generated by the global field Ω with detuning $\delta = \Delta_{\rm p}^{(i,i+1)}/2$, for which

$$\bar{\Delta}_{\rm ls}^{(i)} = \frac{2\Omega^2}{\Delta_{\rm p}^{(i,i+1)}}\left(1 - \sum_{j\neq i}^{N} f_{ij}\right), \tag{D.5}$$

$$J_{ij} = \frac{2\Omega^2}{\Delta_{\rm p}^{(i,i+1)}}\left(1 - f_{ij}\right), \tag{D.6}$$

where $f_{ij} = \left[1 - \frac{\Delta_{\rm p}^{(ij)}}{\Delta_{\rm p}^{(i,i+1)}/2}\right]^{-1}$. The exchange term J_{ij} involves Raman transitions between $|\tilde{r}_i^{(1)}\rangle$ and $|\tilde{r}_j^{(1)}\rangle$ through the ground states $|\tilde{G}\rangle$ with the $2\Omega^2/\Delta_{\rm p}^{(i,i+1)}$ term, and through the $n = 2$ manifolds $|\tilde{r}_{ij}^{(2)}\rangle$ with the $-2\Omega^2 f_{ij}/\Delta_{\rm p}^{(i,i+1)}$ term. The global field Ω also resonantly drives $n = 0 \rightarrow n = 2$ transition with the two-mode squeezing Hamiltonian

$$\hat{H}_2 = \sum_{i=1} \frac{2\Omega^2}{\Delta_{\rm p}^{(i,i+1)}}\left(\hat{\sigma}_+^{(i)}\hat{\sigma}_+^{(i+1)} + \text{h.c.}\right). \tag{D.7}$$

Since we have increased the decay rates $\Gamma_{i\in B} = \Gamma$, the population is driven to the $n_t = 1$ subspace via $\hat{H}_2$ (see figure B1). As illustrated in the inset of figure E1 (a), the atomic dynamics in $n_t = 1$ subspace is dictated by H_{xy}, whose coefficients are fully determined by the ratio $\Delta_{ij}/\Delta_{i,i+1}$ in a scale-invariant fashion (with overall factor $2\Omega^2/\Delta_{\rm p}^{(i,i+1)}$). Generally, let us express the eigenstate $|\epsilon_\mu\rangle$ of H_{xy} in $n_t = 1$ as $|\epsilon_\mu\rangle = \sum_i \alpha_{i,\mu}|\tilde{r}_i^{(1)}\rangle$.

Appendix E. Diagonalization of effective Hamiltonian

For the 1D staggered triangular lattice in figure 1(a), the position vectors are given by $\vec{x}_i = \{(k-1)a_1,\ 0\}$ for odd sites ($i = 2k+1$) and by $\vec{x}_i = \{a_0\cos\theta + (k-1)a_1,\ a_0\sin\theta\}$ for even sites ($i = 2k$), with $\cos\theta = \xi/2$ and $\xi = a_1/a_0$. Under this geometry, the parameter ξ can fully describe the effective Hamiltonian H_{xy}. Figure E1(b) shows the finite-range behavior of the nonlocal coupling rate J_{ij} between $|\tilde{r}_i^{(1)}\rangle \leftrightarrow |\tilde{r}_j^{(1)}\rangle$ in the vdW interacting regime ($p = 6$). For the sufficiently large $\xi > 1$, we find that the rate J_{ij} significantly diminishes for sites $|i-j| > 2$ due to the $\sim 1/r^6$ vdW scaling. In the following discussion, we thereby truncate our analysis up to next-nearest neighbor interactions with the sparse-array H_{xy} as

$$\hat{H}_{xy} = -\sum_{i=1}^{N} \bar{\Delta}_{\rm ls}^{(i)}\hat{\sigma}_{rr}^{(i)} + \sum_{i<j}^{N} J_{ij}\left(\hat{\sigma}_+^{(i)}\hat{\sigma}_-^{(j)} + \text{h.c.}\right), \tag{E.1}$$

with

$$\bar{\Delta}_{\rm ls}^{(i)} = \begin{cases} \frac{J}{2}\times\left(4 + \frac{2}{2-\xi^6} - N\right) & \text{for } i = 1,\ N \\ \frac{J}{2}\times\left(6 + \frac{2}{2-\xi^6} - N\right) & \text{for } i = 2,\ N-1 \\ \frac{J}{2}\times\left(6 + \frac{4}{2-\xi^6} - N\right) & \text{for } 2 < i < N-2, \end{cases} \tag{E.2}$$

$$J_{ij} = \begin{cases} J & \text{for } |i-j| = 1 \\ J\times\left(\frac{1}{2-\xi^6}\right) & \text{for } |i-j| = 2 \\ 0 & \text{for } |i-j| > 2 \end{cases} \tag{E.3}$$

with overall factor $J = 4\Omega^2/\Delta_{\rm p}^{(i,i+1)}$.

Eigenstates $|\epsilon_\mu\rangle = \sum_i \alpha_{i,\mu}|\tilde{r}_i^{(1)}\rangle$ with $\alpha_{i\in B,\mu} = 0$ can be obtained by controlling the ratio between nearest and next-nearest terms for J_{ij} with ξ. As discussed in figure E1(a), this process is analogous to the behavior of coherent population trapping, where destructive quantum interference occurs for the excitation pathways that connects the 'bright' state $|\tilde{r}_i^{(1)}\rangle$ (decay rate $\Gamma \simeq 10^4\Gamma_r$) to 'metastable' states $|\tilde{r}_{j\neq i}^{(1)}\rangle$ (decay rate Γ_r). The emergence of 'dark state' for such a toy model provides an insight on our choice of interaction parameter $\xi \rightarrow \xi_1 = \sqrt[6]{3}$ for symmetric (antisymmetric) eigenstates, whereby $J_{i,i+1} = -J_{i,i+2}$. For instance, in the case of $N = 4$ with

$$\hat{H}_{xy} = \begin{pmatrix} -J & J & -J & 0 \\ J & 0 & J & -J \\ -J & J & 0 & J \\ 0 & -J & J & -J \end{pmatrix}, \tag{E.4}$$

destructive interference in the form $J_{1,2} = -J_{1,3}$ and $J_{2,3} = -J_{3,4}$ occurs for $\alpha_{1,1} = \alpha_{4,1} = 0$. For $N \gg 4$, the eigenstate $|\epsilon_1\rangle$ with $\alpha_{i\in B,1} = 0$ cannot be obtained by locally considering the atoms near the boundaries (i.e.,

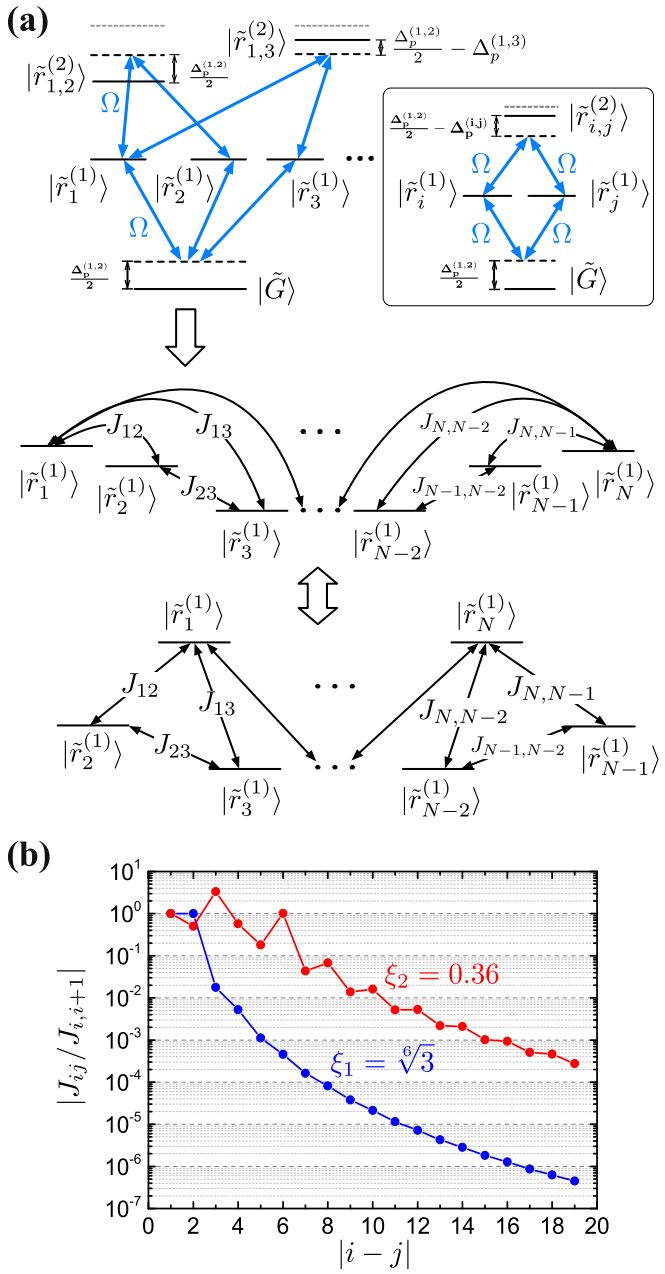

Figure E1. (a) Interaction strength J_{ij} and light shift $\bar{\Delta}^{(i)}_{\rm ls}$ of the effective Hamiltonian H_{xy} are given by Raman transition $|\tilde{r}^{(1)}_i\rangle \leftrightarrow |\tilde{r}^{(1)}_j\rangle$ via two path mediated by $|\tilde{G}\rangle$ and $|\tilde{r}^{(2)}_{i,j}\rangle$. (b) The power law scaling behavior of spin–spin coupling strength J_{ij} with 1D staggered triangular lattices for $\xi_1 = \sqrt[6]{3}$ (blue) and $\xi_2 \simeq 0.36$ (red). For ξ_1, the spatial range of J_{ij} depicts a monotonic power-law decay, whereas jig-jag oscillatory pattern exists for ξ_2.

atoms 1, 2, 3 and $N-2$, $N-1$, N). Instead, the uniqueness of the dark state $|\epsilon_1\rangle$ is a manifestation of the many-body interferences for J_{ij}, $\bar{\Delta}^{(i)}_{\rm ls}$, leading to $\alpha_{i\in B,1} = 0$. Nonetheless, $J_{i,i+1} = -J_{i,i+2}$ provides a reasonable guiding principle for us to guess the dark resonance conditions for atoms near the edges for a certain value of N, due to symmetric sparse characteristics of H_{xy}.

We confirmed this prediction by solving the full spectrum of the sparse Hamiltonian matrix $\hat{H}_{xy}$ with $J_{|i-j|>2} \to 0$ and by numerically simulating the stationary state of the master equation. We obtain two sets of eigenstates $|\epsilon_\mu\rangle = \sum_i \alpha_{i,\mu}|\tilde{r}^{(1)}_i\rangle$ with $\alpha_{1,\mu} = \alpha_{N,\mu} = 0$ for arbitrary N that meets $J_{i,i+1} = -J_{i,i+2}$ at $\xi = \xi_1$ as below

$$\begin{aligned} &\text{set 1}: \quad N = 4 + 6m \ (m = 0, 1, \ldots) \\ &\{\alpha_{i,\mu}\} = \{0, 1, 1, 0, -1, -1, 0, 1, 1, 0, \ldots, -1, -1, 0, 1, 1, 0\}, \end{aligned} \tag{E.5}$$

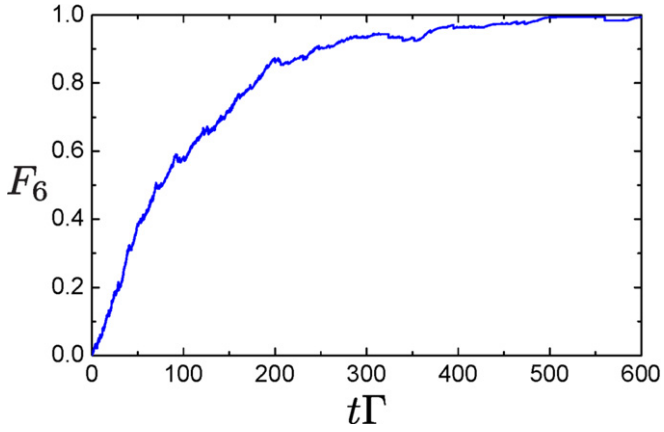

Figure E2. Dynamic formation of steady-state entanglement for $N = 10$ in the extended sample regime. The dark state $|\epsilon_1\rangle$ of the driven-dissipative dynamics is hexapartite entangled, as derived in equations (23) and (24). The entanglement fidelity F_6 is maximized at $(\xi, a_0) = (1.1997, 0.28)$ to $F_6 \to 0.993$.

$$\begin{aligned} \text{set 2} &: \quad N = 6 + 10m \ (m = 0, 1, \ldots) \\ \{\alpha_{i,\mu}\} &= \{0, 1, 1, 1, 1, 0, -1, -1, -1, -1, 0, 1, 1, 1, 1, 0, \ldots \\ &\quad -1, -1, -1, -1, 0, 1, 1, 1, 1, 0\}. \end{aligned} \tag{E.6}$$

Therefore, our method could produce stationary k-partite entanglement in the form of an eigenstate $|\epsilon_1\rangle = |W_k\rangle_A \otimes |g\cdots g\rangle_B$ with $k = 2 + 4m$ (set (E.5)) and $k = 4 + 8m$ (set (E.6)), plotted as blue dots in figure F1 (b). In the main text, we present our numerical result for the Markovian dynamics with the steady state corresponding to set (E.5) (set (E.6)) for figure 2 (figure 3) with $N = 4$ ($N = 6$). In figure E2, we present our result for $N = 10$, thereby producing hexapartite multipartite entanglement in the steady state with fidelity $F > 0.99$. In the hindsight, we can attribute the existence of symmetric entangled steady states in equations (E.5) and (E.6) to the special structure of $\hat{H}_{xy}$. As $\hat{H}_{xy}$ is sparse, highly symmetric, a kind of commensurability requirement is imposed to the eigenstate under the restriction that the coefficients at the edges are zero.

Even if we were to consider the case $J_{|i-j|>2} \neq 0$, our result would not have changed much for $\xi = \xi_1$. The truncation would slightly modify the exact eigenstate as $|\epsilon_i\rangle \to |\epsilon_i\rangle + |\delta\epsilon_i\rangle$ with $\langle\delta\epsilon_i|\epsilon_i\rangle = 0$. Roughly speaking, $\langle\delta\epsilon_i|\delta\epsilon_i\rangle$ scales linear to the energy perturbation up to a leading order. Since the energy perturbation to $\Delta_{\rm p}^{(ij)} \sim 1/r_{ij}^6$ is at most $\delta\Delta_{\rm p} = \Delta_{\rm p}^{(i,i+3)}/\Delta_{\rm p}^{(i,i+1)} \simeq 10^{-2}$ (see figure E1(b)), the perturbation to the entanglement fidelity is at most $\delta F \simeq 10^{-2}$, which is well within the numerical uncertainty of the quantum trajectory method (see figure 3). In terms of dark resonance $J_{i,i+1} = -J_{i,i+2}$, the higher-order interactions $J_{|i-j|>2}$ for $\xi = \xi_1$ (blue dots) are suppressed by at least 10^2 relative to $J_{i,i+1}$, $J_{i,i+2}$. By taking $N \to \infty$, the higher-order contributions $\sum_{x>2}^{\infty}|J_{i,i+x}|$ would still be far too negligible to have any impact on the final state with $\sum_{x>2}^{\infty}|J_{i,i+x}| \ll 10^{-2} \times \min(|J_{i,i+1}|, |J_{i,i+2}|)$, leading to $F \simeq 0.99$.

The infinitesimally reduced fidelity can then be recovered to $F \to 1$ by displacing ξ to an optimal value by the more general condition $J_{1,2} = -\sum_{x\geqslant 2}\alpha_{x,1}J_{1,1+x}$ for $|\epsilon_1\rangle$ at the expense of having a slightly modified steady states, i.e., a new eigenstate $|\epsilon_1'\rangle = |W'\rangle_A \otimes |g\cdots g\rangle_B$. Due to the inherent symmetry of the system, this modified steady state $|W'\rangle$ would only marginally differ from the original one. Furthermore, the original steady state $|\epsilon_1\rangle$ could be recovered by re-adjusting the arrangement of the atoms. In any case, the only sensitive parameter that determines the optimal fidelity is the 'branching' ratio $\Gamma_r/\Gamma \simeq 10^{-4}$, which sets the balance between the lifetimes for dissipative and coherent evolutions, thereby the final fidelity $F \sim 1 - \mathcal{O}(\Gamma_r/\Gamma)$.

On the other hand, in the region of $\xi \ll 1$ ($J_{|i-j|>2} \geqslant J_{|i-j|=1}, J_{|i-j|=2}$), the optimal value ξ cannot be predicted by the dark resonance conditions of the sparse-array matrix H_{xy}. In this case, J_{ij} displays zigzag oscillatory decay as shown in figure E1(b), and higher-order terms $J_{|i-j|>2}$ must be included in the analysis.

Appendix F. *N*-partite uncertainty witness

In this section, we describe our method of constructing the N-partite uncertainty witness [46]. Our entanglement witness $\{\Delta, \gamma_c\}$ consists of identifying the boundaries $\Delta_b^{(k-1)}$ for all possible states $\hat{\rho}_b^{(k-1)}$ produced by convex combinations of pure $(k-1)$-partite entangled states $|\psi_b^{(k-1)}\rangle$ as well as their mixed siblings with less k. As shown in [46], the lower bound of $\Delta_b^{(k-1)}$ is attained by taking a convex set of $\{\Delta_b(\hat{\rho}_b^{(k-1)}), \gamma_c(\hat{\rho}_b^{(k-1)})\}$ for all pure states $\hat{\rho}_b^{(k-1)} = |\psi_b^{(k-1)}\rangle\langle\psi_b^{(k-1)}|$. In figure 3, we depict the boundaries

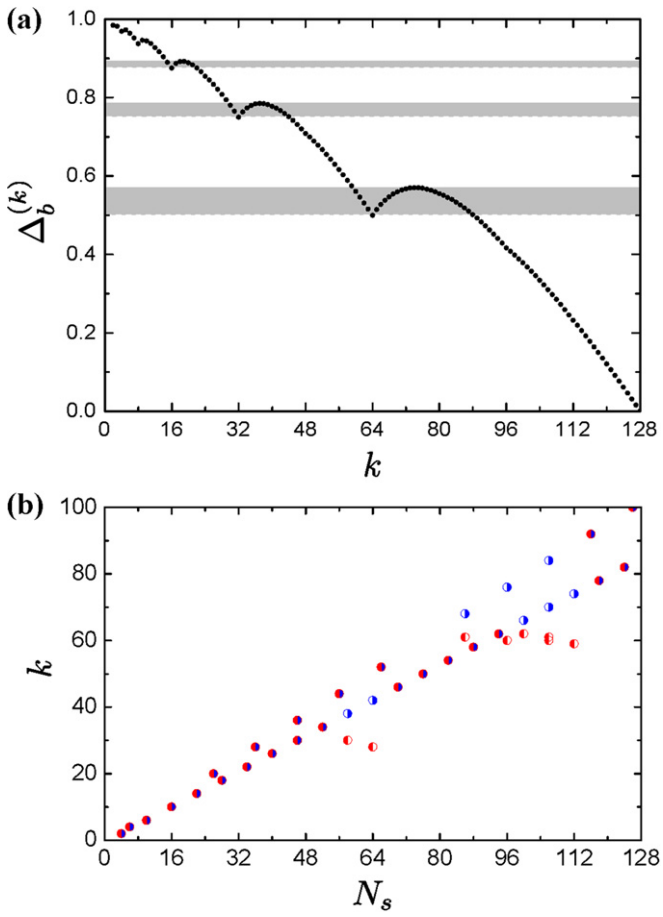

Figure F1. (a) k-partite uncertainty bounds $\Delta_b^{(k)}$ for $k \in \{1, \ldots, 128\}$ and N_m=128. Shaded regions indicate the parameter spaces for which ambiguity exists for $\Delta_b^{(k)} \not> \Delta_b^{(k+1)}$, due to the nonlinear sensitivity of Δ. For such regions, we conservatively quote the minimum value k_m for the genuine k-partite entanglement with $\Delta(\hat{\rho}) < \Delta_b^{(k_m)}$. (b) The minimum entanglement depth k_m certified by $\{\Delta, y_c\}$ (red dots), and the entanglement depth k in the purported eigenstate $|\epsilon_1\rangle = |W_k\rangle_A \otimes |g\cdots g\rangle_B$ (blue dots), with fully balanced k-partite W state $|W_k\rangle_A$.

$\Delta_b^{(1)}$, $\Delta_b^{(2)}$, $\Delta_b^{(3)}$ for all possible realizations of fully separable states, bipartite entangled and tripartite entangled states, respectively, by following the procedures of [47, 48].

Generally, we can determine the projection operators $\hat{\Pi}_i = |W_i\rangle\langle W_i|$ with $i \in \{1, \ldots, 2^m\}$ for arbitrary number of systems $N_m = 2^m$ with the recursive relationship

$$|W_i^{(m)}\rangle = \frac{1}{\sqrt{2}}\left(\left|W_i^{(m-1)}, \tilde{G}^{(m-1)}\right\rangle \pm \left|\tilde{G}^{(m-1)}, W_i^{(m-1)}\right\rangle\right),$$

from the initial condition $|W_{1,2}^{(1)}\rangle = 1/\sqrt{2}\,(|gr\rangle \pm |rg\rangle)$. Here, $|W_i^{(m)}\rangle = (1/\sqrt{2^m})\sum_i^{2^m}|\tilde{r}_i^{(1)}\rangle$ and $|\tilde{G}^{(m)}\rangle = |g\cdots g\rangle$ for N_m atoms. As discussed in [46], we then construct the uncertainty witness $\Delta = \sum_i \langle\delta^2\hat{\Pi}_i\rangle$ to identify the bounds $\{\Delta_b^{(k-1)}\}$ for $(k-1)$-partite entanglement up to $k \leqslant N_m$. For convenience, we set the maximal $N_m \geqslant N_A$ to be larger than the number N_A of atoms in A, so that we could distinguish the entanglement depth k for any $k \leqslant N_A$.

For figure 4, we assumed the stationary limit, so that $y_c \to 0$. In order to verify the minimum bounds $\Delta_b^{(k-1)}$, we only need to optimize the overlap of pure $(k-1)$-partite entangled states of the form $|\psi_b^{(k-1)}\rangle = |\tilde{G}^{(N-k+1)}\rangle \otimes \sum_i^{k-1}\alpha_i|\tilde{r}_i^{(1)}\rangle$ with one of the projectors $|W_i\rangle$. This is achieved when the test state is a balanced $(k-1)$-partite W-state (i.e., $|\alpha_i| = 1/\sqrt{k-1}$). Figure F1 depicts the uncertainty bounds $\Delta_b^{(k-1)}$ with $k \in \{1, \ldots, N_m\}$ calculated for $y_c = 0$ and $N_m = 2^7 = 128$. The shaded regions represent the parameter spaces for which ambiguity exists for the tiered structure $\Delta_b^{(k)} \not> \Delta_b^{(k+1)}$. This is caused by the nonlinear structure of $\Delta(|\psi_b^{(k)}\rangle\langle\psi_b^{(k)}|)$ to POVM values $\hat{\Pi}_i$. For such regions, we conservatively quote the minimum value of k_m and certify the presence of genuine entanglement depth $k_m + 1$ stored in the purported state $\hat{\rho}$ with $\Delta(\hat{\rho}) < \Delta_b^{(k_m)}$ (see figure F1(b)).Hence, the entanglement depth k_m (red dot) is a conservative estimate, which can be detected in an experiment, as opposed to the model-dependent analysis of k (blue dot) for the pure state form $|\epsilon_1\rangle = |W_k\rangle_A \otimes |g\cdots g\rangle_B$ (i.e., by counting the number of non-zero probability amplitudes in $|W_k\rangle_A$).

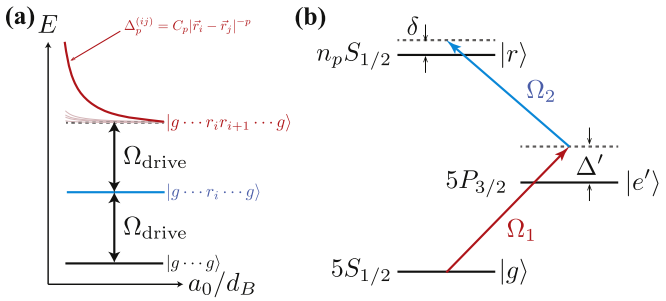

Figure G1. (a) N-atom Rydberg blockade. Effective Rabi frequency between $|g\rangle$ and $|r\rangle$ is given by Ω. (b) Level diagram for ^{85}Rb atom. The effective transition between $|g\rangle$ and $|r\rangle$ is formed by a two-photon transition via the intermediate excited state $|e'\rangle$, with $|g\rangle = |5S_{1/2}\rangle$, $|e'\rangle = |5P_{3/2}\rangle$, and $|r\rangle = |n_pS_{1/2}\rangle$. Δ' is the one-photon detuning respect to $|e'\rangle$ by field Ω_1 ($\lambda_1 \simeq 474$ nm) and δ is the two-photon detuning by the field Ω_2 ($\lambda_2 \simeq 795$ nm).

Appendix G. Experimental parameters with alkali atoms

Let us consider ^{85}Rb atoms interacting with optical field near the transition between $|g\rangle = |5S_{1/2}\rangle$ and $|r\rangle = |n_pS_{1/2}\rangle$ with two-photon Rabi frequency $\Omega = \Omega_1\Omega_2/\Delta'$ and detuning δ that globally addresses the atomic sample. As shown by figure G1, this could be achieved by a two-photon transition with Rabi frequencies Ω_1, Ω_2 via the intermediate state $|e'\rangle = |5P_{3/2}\rangle$ with one-photon detuning Δ'. The Rydberg excitation spectrum displays a highly nonlinear excitation spectrum n due to the dipole–dipole interaction $\Delta_p^{(ij)} = C_p|\vec{r}_i - \vec{r}_j|^{-p}$, with the most shifted level given by configuration states consisting of nearest-neighbor excitations $|\tilde{r}_{i,i+1}^{(2)}\rangle$ with $\Delta_p^{(i,i+1)}$.

In order to achieve the parameter sets of figures 2–4, we take the principal quantum number $n_p = 100$ so that $|r\rangle = |100S_{1/2}, m_j = 1/2\rangle$. The radiative lifetime is given by $\tau = \tau_0(n_p^*)^\alpha$, where $n_p^* = n_p - \delta_{nl}$ is the effective principal number and δ_{nl} is the quantum defect. With $\tau_0 = 1.43$ ns and $\alpha = 2.94$ for $|100S_{1/2}\rangle$ [24], we find that the Rydberg lifetime is $\tau_r = 1$ ms (i.e., $\Gamma_r \simeq 1$ kHz). On the other hand, $\Gamma_e \simeq 38$ MHz for $|e\rangle$. Since $\Gamma \to \Gamma_e$ in the limit of strong dressing fields Ω_1 for 'reservoir' atoms, $\Gamma \to 10^4\Gamma_r$ can be achieved in an experiment.

By setting $\Omega_{1,2} = 10$ GHz and $\Delta' = 10\Omega_{1,2}$ (i.e., $\Omega = 1$ GHz), the photo-ionization rate can be determined by

$$\gamma_\pi = \frac{I}{\hbar w} \times \sigma_\pi = \frac{2I_{\rm sat}}{\hbar w}\left(\frac{\Omega_{1,2}}{\Gamma_e'}\right)^2 \sigma_\pi, \tag{G.1}$$

where $\Gamma_e' = 38$ MHz is the spontaneous decay rate for $|e'\rangle$, $I_{\rm sat} = 4.5$ mW cm^{-2} is the saturation intensity for $|g\rangle \to |e'\rangle$ and $\sigma_\pi \leqslant 2 \times 10^{-7}$ Å^2 is the photo-ionization cross-section that couples the Rydberg state $|100S_{1/2}\rangle$ to the continuum free-electron wavefunctions [24]. Hence, we find that the photo-ionization lifetime is limited to $\tau_\pi = 1/\gamma_\pi \gg 10$ ms $\gg 1/\Gamma_r$ [54].

The blockade shift $\Delta_p^{(ij)}$ is determined by Rydberg coefficient C_p, for which we take $C_6 = 56$ THz μm^6 for the vdW interaction between two Rydberg atoms in $|r\rangle = |100S_{1/2}, m_j = 1/2\rangle$ [50–53]. For $\Omega = 1$ GHz and $N = 6$, the blockade shift for nearest-neighbors is $\Delta_6^{(i,i+1)} = 800$ GHz ($a_0/d_B \simeq 0.35$), while the power-broadened linewidth for the transition $|g\rangle \leftrightarrow |r\rangle$ *is* $w_d \simeq \sqrt{2}\,\Omega$. The resulting blockade radius is $d_B \simeq \sqrt[6]{C_6/w_d} = 5.8$ and $1.9(2.3)$ μm $\leqslant a_0(a_1) \leqslant 2.1(2.5)$ μm for $F_4 \simeq 0.99$. In terms of spatial localizations, the variance of the lattice constants would need to be less than δa_0, $\delta a_1 \leqslant 200$ nm in order to achieve $F_4 \simeq 0.99$. This could be readily achieved in deep optical lattice experiments with zero-point motion $\delta x \sim 10$ nm [70]. Hence, Rydberg atoms interacting in the strong blockade regime with the lattice constants a_0, $a_1 \simeq 1$ μm $> \lambda_0/2$ (figures 2–4) can be spatially resolved, so that Ω_d can be locally addressed to the reservoir sites without the requirement for diffraction-limited imaging resolutions $\lambda_0/2$ [71]. Therefore, the pumping time for $F_4 \simeq 0.99$ for $N = 6$ is then $t_p \sim 6 \times 10^2/\Gamma = 60$ μs, which is not limited by the photo-ionization time $\tau_\pi \gg 10$ ms.

In addition, if we reduce the fidelity threshold $F_4 \to 0.9(\Gamma_r/\Gamma = 10^{-3})$, the steady state can be achieved within $t_p = 600$ μs $\ll 1$s $\ll t_\pi$ for relaxed parameters $\Gamma = 1$ MHz, $\Omega = 50$ MHz, and $d_B = 9.6$ μm over the region of $3.8(4.5)$ μm $\leqslant a_0(a_1) \leqslant 3.9(4.7)$ μm as shown in table G1. Since the quantum jumps in the $n = 1$ subspace occur on a time-scale of $t_j \sim \mathcal{O}(N^2)$ due to the random walk for $|\tilde{r}_i^{(1)}\rangle$ until it reaches the 'reservoir' sites with $\Gamma_{1,N} = \Gamma \gg \Gamma_r$, we expect that the pumping time to reach stationarity also scales as $t_p \sim \mathcal{O}(N^2)$. On the other hand, if we were to address every 'zeros' in equations (E.5) and (E.6) with Ω_d, the pumping time

Table G1. Summary of experimental parameters to achieve steady-state entanglement with fidelity F_4 for ^{85}Rb. The set of parameters are given by Rydberg state $|r\rangle = |100S_{1/2}\rangle$ with decay rate $\Gamma_r = 1$ kHz, decohering state $|e\rangle = |5P_{1/2}\rangle$ with $\Gamma_e = 36$ MHz, and van der Waals coefficient $|C_6| = 56$ THz μm^6. The error bars in a_0, a_1 indicate the range of lattice constants, which allow robust entanglement production with $F_4 > 0.9$.

Γ/Γ_r	Ω/Γ	F_4	Ω (MHz)	d_B (μm)	a_0 (μm)	a_1 (μm)	t_p (μs)
10^4	10^3	0.99	10^4	4.0	$1.1^{+0.7}_{-0.4}$	$1.4^{+0.8}_{-0.5}$	20
10^4	10^2	0.99	10^3	5.8	$2.0^{+0.6}_{-0.5}$	$2.4^{+0.7}_{-0.6}$	20
10^4	50	0.98	5.0×10^2	6.6	$2.4^{+0.5}_{-0.4}$	$2.9^{+0.6}_{-0.5}$	30
10^4	30	0.97	3.0×10^2	7.1	$2.7^{+0.5}_{-0.3}$	$3.3^{+0.6}_{-0.3}$	40
10^4	15	0.92	1.5×10^2	8.0	$3.3^{+0.2}_{-0.2}$	$3.9^{+0.2}_{-0.2}$	55
10^3	100	0.92	10^2	8.6	$3.3^{+0.3}_{-0.4}$	$3.9^{+0.5}_{-0.4}$	400
10^3	50	0.91	50	9.6	$3.8^{+0.1}_{-0.1}$	$4.6^{+0.1}_{-0.1}$	600

Table G2. Summary of experimental parameters to achieve steady-state entanglement with fidelity F_4 for ^{133} Cs. The set of parameters are given by Rydberg state $|r\rangle = |100P_{3/2}\rangle$ with decay rate $\Gamma_r = 330$ Hz, decohering state $|e\rangle = |7S_{1/2}\rangle$ with $\Gamma_e \sim 36$ MHz, and van der Waals coefficient $|C_6| = 88$ THz μm^6. The error bars in a_0, a_1 indicate the range of lattice constants, which allow robust entanglement production with $F_4 > 0.9$.

Γ/Γ_r	Ω/Γ	F_4	Ω (MHz)	d_B (μm)	a_0 (μm)	a_1 (μm)	t_p (μs)
10^4	10^3	0.99	3.3×10^3	5.2	$1.5^{+0.8}_{-0.5}$	$1.8^{+1.0}_{-0.6}$	60
10^4	10^2	0.99	3.3×10^2	7.6	$2.7^{+0.8}_{-0.6}$	$3.2^{+0.9}_{-0.7}$	60
10^4	50	0.98	1.7×10^2	8.5	$3.1^{+0.7}_{-0.5}$	$3.8^{+0.8}_{-0.6}$	90
10^4	30	0.97	10^2	9.2	$3.5^{+0.6}_{-0.4}$	$4.2^{+0.8}_{-0.4}$	120
10^4	15	0.92	50	10	$4.3^{+0.2}_{-0.2}$	$5.1^{+0.2}_{-0.2}$	160
3×10^3	10^2	0.96	10^2	9.2	$3.5^{+0.4}_{-0.4}$	$4.2^{+0.6}_{-0.4}$	210
10^3	10^2	0.92	33	11	$4.2^{+0.6}_{-0.4}$	$5.1^{+0.7}_{-0.5}$	1200
10^3	50	0.91	17	13	$5.0^{+0.1}_{-0.1}$	$6.0^{+0.1}_{-0.1}$	1800

$t_p \sim \mathcal{O}(N)$ will scale linear to the number N of eigenstates $\{|\epsilon_\mu\rangle\}$ spanning $n = 1$. Hence, even for $N = 126$ atoms with $(a_0, a_1) \simeq (0.9, 1\ \mu\text{m})$, the condition $\Delta_p^{(1,N-1)} + \Delta_p^{(2,N-1)} > w_d^{(2)}$ is satisfied so that the atomic sample can efficiently relax into the steady state $|\epsilon_1\rangle$.

We have also considered the case for ^{133} Cs where direct UV excitation to $|r\rangle = |100P_{3/2}\rangle$ state is possible [55]. We set the decohering state to $|e\rangle = |7S_{1/2}\rangle$ ($\Gamma_e \simeq 36$ MHz). Because $|100P_{3/2}\rangle$ offers lower $\Gamma_r \to 330$ Hz [24], the steady-state entanglement fidelity $F \sim 1 - \mathcal{O}(\Gamma_r/\Gamma)$ can be improved relative to the case of $|100S_{1/2}\rangle$ with the fixed parameters in table G2 . For example, if we choose $\Omega = 50$ MHz and $\Gamma = 1$ MHz as above, the resulting fidelity for $N = 6$is $F_4(|100P_{3/2}\rangle) = 0.96 > F_4(|100S_{1/2}\rangle) = 0.91$. The resulting lattice constants for $N = 126$ atoms are $(a_0, a_1) \simeq (1.0, 1.2\mu\text{m}) \gtrsim 1\ \mu$m so that they are optically addressable, thereby allowing for steady-state hectapartite entanglement. The photo-ionization lifetime may also be significantly improved, as demonstrated in [55].

In conclusion, we estimate that our method could be extended to generate 100-partite entangled steady states with the parameters $\{\Omega_{1,2}, \delta, \Delta', |g\rangle, |e'\rangle, |r\rangle\}$. Further improvement in the entanglement depth k may be possible by optimizing the driving field Ω under the constraint $\frac{2\Omega^2}{\delta} \gg \Gamma_r$ for a given $|r\rangle$, which reduces the ionization time t_π [54]. Alternative strategies, including the use of photonic crystals with atoms in low-lying electronic states, will be discussed elsewhere.

References

[1] Amico L, Fazio R, Osterloh A and Vedral V 2008 Entanglement in many-body systems *Rev. Mod. Phys.* **80** 517
[2] Diehl S, Micheli A, Kantian A, Kraus B, Büchler H P and Zoller P 2008 Quantum states and phases in driven open quantum systems with cold atoms *Nat. Phys.* **4** 878
[3] Verstraete F, Wolf M M and Cirac J I 2009 Quantum computation and quantum-state engineering driven by dissipation *Nat. Phys.* **5** 633
[4] Kastoryano M J, Wolf M M and Eisert J 2013 Precisely timing dissipative quantum information processing *Phys. Rev. Lett.* **110** 110501
[5] Campisi M, Hänggi P and Talkner P 2011 Colloquium: quantum fluctuation relations: foundations and applications *Rev. Mod. Phys.* **83** 771
[6] Plenio M B, Huelga S F, Beige A and Knight P L 1999 Cavity-loss-induced generation of entangled atoms *Phys. Rev.* A **59** 2468
[7] Schneider S and Milburn G J 2002 Entanglement in the steady state of a collective-angular-momentum (Dicke) model *Phys. Rev.* A **65** 042107

[8] Plenio M B and Huelga S F 2002 Entangled light from white noise *Phys. Rev. Lett.* **88** 197901
[9] Braun D 2002 Creation of entanglement by interaction with a common heat bath *Phys. Rev. Lett.* **89** 277901
[10] Jakóbczyk L 2002 Entangling two qubits by dissipation *J. Phys. A: Math. Gen.* **35** 6383
[11] Kraus B, Büchler H P, Diehl S, Kantian A, Micheli A and Zoller P 2008 Preparation of entangled states by quantum Markov processes *Phys. Rev.* A **78** 042307
[12] Muschik C A, Polzik E S and Cirac J I 2011 Dissipatively driven entanglement of two macroscopic atomic ensembles *Phys. Rev.* A **83** 052312
[13] Kastoryano M J, Reiter F and Sørensen A S 2011 Dissipative preparation of entanglement in optical cavities *Phys. Rev. Lett.* **106** 090502
[14] Cho J, Bose S and Kim M S 2011 Optical pumping into many-body entanglement *Phys. Rev. Lett.* **106** 020504
[15] Vollbrecht K G H, Muschik C A and Cirac J I 2011 Entanglement distillation by dissipation and continuous quantum repeaters *Phys. Rev. Lett.* **107** 120502
[16] Krauter H, Muschik C A, Jensen K, Wasilewski W, Petersen J M, Cirac J I and Polzik E S 2011 Entanglement generated by dissipation and steady state entanglement of two macroscopic objects *Phys. Rev. Lett.* **107** 080503
[17] Lin Y *et al* 2013 Dissipative production of a maximally entangled steady state of two quantum bits *Nature* **504** 415
[18] Shanker S *et al* 2013 Autonomously stabilized entanglement between two superconducting quantum bits *Nature* **504** 419
[19] Barreiro J T *et al* 2011 An open-system quantum simulator with trapped ions *Nature* **470** 486
[20] Schindler P *et al* 2013 Quantum simulation of dynamical maps with trapped ions *Nat. Phys.* **9** 361
[21] Jaksch D, Cirac J I, Zoller P, Rolston S L, Côté R and Lukin M D 2000 Fast quantum gates for neutral atoms *Phys. Rev. Lett.* **85** 2208
[22] Lukin M D *et al* 2001 Dipole blockade and quantum information processing in mesoscopic atomic ensembles *Phys. Rev. Lett.* **87** 037901
[23] Saffman M, Walker T G and Mølmer K 2010 Quantum information with Rydberg atoms *Rev. Mod. Phys.* **82** 2313
[24] Gallagher T F 1994 *Rydberg Atoms* (Cambridge: Cambridge University Press)
[25] Rao D D B and Mølmer K 2013 Dark entangled steady states of interacting Rydberg atoms *Phys. Rev. Lett.* **111** 033606
[26] Carr A W and Saffman M 2013 Preparation of entangled and anti-ferromagnetic states by dissipative Rydberg pumping *Phys. Rev. Lett.* **111** 033607
[27] Olmos B, González-Férez R and Lesanovsky I 2009 Fermionic collective excitations in a lattice gas of Rydberg atoms *Phys. Rev. Lett.* **103** 185302
[28] Weimer H, Müller M, Lesanovsky I, Zoller P and Büchler H P 2010 A Rydberg quantum simulator *Nat. Phys.* **6** 382
[29] Lee T E, Häffner H and Cross M C 2012 Collective quantum jumps of Rydberg atoms *Phys. Rev. Lett.* **108** 023602
[30] Zhao B, Glaetzle A W, Pupillo G and Zoller P 2012 Atomic Rydberg reservoirs for polar molecules *Phys. Rev. Lett.* **108** 193007
[31] Ates C, Olmos B, Li W and Lesanovsky I 2012 Dissipative binding of lattice bosons through distance-selective pair loss *Phys. Rev. Lett.* **109** 233003
[32] Glaetzle A W, Nath R, Zhao B, Pupillo G and Zoller P 2012 Driven-dissipative dynamics of a strongly interacting Rydberg gas *Phys. Rev.* A **86** 043403
[33] Höning M, Muth D, Petrosyan D and Fleischhauer M 2013 Steady-state crystallization of Rydberg excitations in an optically driven lattice gas *Phys. Rev.* A **87** 023401
[34] Lesanovsky I and Garrahan J P 2013 Kinetic constraints, hierarchical relaxation, and onset of glassiness in strongly interacting and dissipative Rydberg gases *Phys. Rev. Lett.* **111** 215305
[35] Petrosyan D, Höning M and Fleischhauer M 2013 Spatial correlations of Rydberg excitations in optically driven atomic ensembles *Phys. Rev.* A **87** 053414
[36] Wilk T *et al* 2010 Entanglement of two individual neutral atoms using Rydberg blockade *Phys. Rev. Lett.* **104** 010502
[37] Isenhower L *et al* 2010 Demonstration of a neutral atom controlled-NOT quantum gate *Phys. Rev. Lett.* **104** 010503
[38] Schauß P *et al* 2012 Observation of spatially ordered structures in a two-dimensional Rydberg gas *Nature* **491** 87
[39] Dudin Y O and Kuzmich A 2012 Strongly interacting Rydberg excitations of a cold atomic gas *Science* **336** 887
[40] Peyronel T *et al* 2012 Quantum nonlinear optics with single photons enabled by strongly interacting atoms *Nature* **488** 57
[41] Schempp H *et al* 2014 Full counting statistics of laser excited Rydberg aggregates in a one-dimensional geometry *Phys. Rev. Lett.* **112** 013002
[42] Gühne O and Toth G 2009 Entanglement detection *Phys. Rep.* **474** 1
[43] Sørensen A S and Mølmer K 2001 Entanglement and extreme spin squeezing *Phys. Rev. Lett.* **86** 4431
[44] Hofmann H F and Takeuchi S 2003 Violation of local uncertainty relations as a signature of entanglement *Phys. Rev.* A **68** 032103
[45] Duan L-M 2011 Entanglement detection in the vicinity of arbitrary Dicke states *Phys. Rev. Lett.* **107** 180502
[46] Lougovski P, van Enk S J, Choi K S, Papp S B, Deng H and Kimble H J 2009 Verifying multipartite mode entanglement of W states *New J. Phys.* **11** 063029
[47] Papp S B, Choi K S, Deng H, Lougovski P, van Enk S J and Kimble H J 2009 Characterization of multipartite entanglement for one photon shared among four optical modes *Science* **324** 764
[48] Choi K S, Goban A, Papp S B, van Enk S J and Kimble H J 2010 Entanglement of spin waves among four quantum memories *Nature* **468** 412
[49] Lewenstein M, Cirac J I and Zoller P 1995 Master equation for sympathetic cooling of trapped particles *Phys. Rev.* A **51** 4617
[50] Singer K, Stanojevic J, Weidemüller M and Côté R 2005 Long-range interactions between alkali Rydberg atom pairs correlated to the ns–ns, np–np and nd–nd asymptotes *J. Phys. B: At. Mol. Opt. Phys.* **38** S295
[51] Walker T G and Saffman M 2008 Consequences of Zeeman degeneracy for the van der Waals blockade between Rydberg atoms *Phys. Rev.* A **77** 032723
[52] Dudin Y O, Li L, Bariani F and Kuzmich A 2010 Observation of coherent many-body Rabi oscillations *Nat. Phys.* **8** 790
[53] Balewski J B *et al* 2013 Coupling a single electron to a Bose–Einstein condensate *Nature* **502** 664
[54] Saffman M and Walker T G 2005 Analysis of a quantum logic device based on dipole–dipole interactions of optically trapped Rydberg atoms *Phys. Rev.* A **72** 022347
[55] Hankin A M *et al* 2014 Two-atom Rydberg blockade using direct 6S to nP excitation *Phys. Rev.* A **89** 033416
[56] Grünzweig T, Hilliard A, McGovern M and Andersen M F 2010 Near-deterministic preparation of a single atom in an optical microtrap *Nat. Phys.* **6** 951
[57] Jo G, Guzman J, Thomas C K, Hosur P, Vishwanath A and Stamper-Kurn D M 2012 Ultracold atoms in a tunable optical Kagome lattice *Phys. Rev. Lett.* **108** 045305
[58] Barredo D *et al* 2014 Demonstration of a strong Rydberg blockade in three-atom systems with anisotropic interactions *Phys. Rev. Lett.* **112** 183002
[59] Shahmoom E and Kurizki G 2013 Non-radiative interaction and entanglement between distant atoms *Phys. Rev.* A **87** 033831

[60] Douglas J S et al 2015 Quantum many-body models with cold atoms coupled to photonic crystals Nat. Photonics 9 326
[61] Goban A et al 2014 Atom-light interactions in photonic crystals Nat. Commun. 5 3808
[62] Lieb E H and Robinson D W 1972 The finite group velocity of quantum spin systems Commun. Math. Phys. 28 251
[63] Eisert J, van den Worm M, Manmana S R and Kastner M 2013 Breakdown of quasi-locality in long-range quantum lattice models Phys. Rev. Lett. 111 260401
[64] Lee S K et al 2015 Localization and diffusion of many-body entanglement in long-range interacting disordered lattice spin models in preparation
[65] Childs A M, Gosset D and Webb Z 2013 Universal computation by multiparticle quantum walk Science 339 791
[66] Heaney L, Cabello A, Santos M F and Vedral V 2011 Extreme nonlocality with one photon New J. Phys. 13 053054
[67] Rao D D B and Mølmer K 2014 Deterministic entanglement of Rydberg ensembles by engineered dissipation Phys. Rev. A 90 062319
[68] Reiter F, Reeb D and Sørensen A S 2015 Scalable dissipative preparation of many-body entanglement preprint (arXiv:1501.06611)
[69] James D F V and Jerke J 2007 Effective Hamiltonian theory and its applications in quantum information Can. J. Phys. 85 625
[70] Goban A et al 2012 Demonstration of a state-insensitive, compensated nanofiber trap Phys. Rev. Lett. 109 033603
[71] Bakr W S, Gillen J I, Peng A, Fölling S and Greiner M 2009 A quantum gas microscope for detecting single atoms in a Hubbard-regime optical lattice Nature 462 74